MLM--2998

DE83 002812

MLM-2998
UC-4 and UC-22

Mound Activities in Chemical and Physical Research: January-June 1982

Issued: October 25, 1982

MOUND FACILITY
Miamisburg, Ohio 45342

operated by
MONSANTO RESEARCH CORPORATION
a subsidiary of Monsanto Company

for the
U. S. DEPARTMENT OF ENERGY

Contract No. DE-AC04-76-DP00053

Foreword

This report is issued semiannually by Mound. Under the sponsorship of the DOE Division of Basic Energy Sciences, Mound is responsible for research in the physical sciences to further the progress of science and technology in the public interest. This report is submitted by B. R. Kokenge, Director of Nuclear Operations, and R. E. Vallee, Manager of Technology Applications and Development, from contributions prepared by W. M. Rutherford, Science Fellow (Thermal Diffusion) W. L. Taylor, Science Fellow (Gas Dynamics and Cryogenics); G. L. Silver, Science Fellow (Separation Chemistry); L. J. Wittenberg, Leader, Metal Hydride Research; and from members of the Isotope Separation Section: W. R. Wilkes, Isotope Separation Manager; E. D. Michaels, Leader, Isotope Separation Engineering; and B. E. Jepson Senior Research Specialist, Metal Isotope Separation Research and Development.

These reports are not intended to constitute publication in any sense of the word. Final results either will be submitted for publication in regular professional journals or will be published in the form of MLM topical reports.

Previous reports in this series are:

MLM-2241	MLM-2590
MLM-2296	MLM-2654
MLM-2354	MLM-2727
MLM-2414	MLM-2756
MLM-2450	MLM-2809
MLM-2506	MLM-2884
MLM-2555	MLM-2892

Contents

I. Low temperature research

II. Separation research

The 45 cm research column was used to measure bromine isotope separation in bromotrifluoromethane. A small separation was found, but it was not judged to be large enough to support use of the compound as a working fluid for bromine isotope separation in the 13-column experimental cascade.

Enriched ^{79}Br was separated by liquid phase thermal diffusion of bromobenzene in the 13-column experimental cascade. A total of 88 g of ^{79}Br enriched to 90.6% was accumulated at an average rate of 0.43 g/day.

Low temperature research

Reaction rates of deuterium-tritium mixtures

G. T. McConville, D. A. Menke, and R. E. Ellefson

The rate of reaction experiments of D_2+T_2 described in previous progress reports [1-3] is continuing to yield interesting and at times surprising results. In the last report, the pressure dependence of the rate was shown to indicate a gas phase reaction. In the present report, the pressure dependent data are reduced to yields of DT molecules per ion pair. Also in the last report, the effect of the impurity CT_4 as an inhibitor for the reaction was shown. We now give further data for CT_4 and also T_2O as impurities.

The only other measurements of β-induced reaction of D_2 and T_2 are those of Pyper, et al [1]. The reaction of H_2 and T_2 has been studied by Dorfman, et al [2-4]. They indicated that the reaction was a complex chain reaction that could be described by a first order equation. Thompson and Schaeffer [5,6] showed that, since the radiation induced H_2+D_2 reaction rate can be drastically reduced by the addition of small amounts of Kr or Xe, the reaction must proceed by a chain of ion-molecule interactions. Dorfman and Shipko [4], using a very clean glass system, have shown that the yields with low radiation intensities can be as high as 2×10^4 molecules per 100 eV. In the one experiment with a high T_2 concentration (70% H_2, 30% T_2), the yield is 4.7×10^3 (HT) molecules/100 eV. This T_2 concentration is comparable to the present experiments.

The reaction rates were measured in a specially constructed stainless steel container. The mixing cell was constructed, cleaned, and treated (by Quantum Mechanics, Inc.) [7] to produce a non-reactive surface. The cell was transferred to this laboratory under high vacuum. The evidence given by Quantum Mechanics that the treated surface is non-reactive is that a H_2+D_2 mixture was stored in a comparable container for a year with no detectable HD appearing in the mixtures [8]. The treatment reduces the iron content in the surface layer and depletes protium from the container walls. The container was exposed to an atmosphere in putting it in our system leading to a chrome-nickel oxide barrier layer on the surface to the penetrations of hydrogen isotopes. The mixing cell was described in reference 2.

The mass spectrometric analysis indicated that the initial D_2 and T_2 were very clean. The only detectable impurity (to within 0.003%) in the D_2 supply was approximately 0.2% HD. The only detectable chemical impurity in the T_2 supply was ^3He, which increased as the experiments progressed from 3% to 4%. After mixing, the ^3He concentration was approximately 1.0 to 1.4%. There was 0.2% HT and from 0.3 to 0.4% DT in each starting T_2 sample.

Measurements of the reaction rate at a total pressure of 300 torr were made with T_2 concentrations of 10, 30, 50, 60, 75 and 90%. Using 30% T_2 mixtures, measurements were made at total pressures of 20, 40, 150, 300 and 500 torr. Dorfman and Mattraw [2] showed their rates could be described by:

$$(HT)_\infty - (HT)_t = (HT)_\infty e^{-kt}, \qquad (1)$$

but with up to 10% HT in their starting samples, their plots of $1-\frac{HT_t}{HT_\infty}$ did not go through at t = 0. We find, if we subtract the small initial DT concentration from DT(t) and DT (∞), all measurements could be represented by:

$$\ell nQ = \ell n[1 - \frac{DT(t)-DT(o)}{DT(\infty)-DT(o)}] = kt \qquad (2)$$

where the resulting line, going through 1 at t = 0, was straight over as much as 98% of the reaction. The decay of T_2 and D_2 in the samples are then represented by:

$$\ell nQ = \ell n\left[\frac{D_2(t)-D_2(\infty)}{D_2(o)-D_2(\infty)}\right] = kt \qquad (3)$$

$$\ell nQ = \ell n\left[\frac{T_2(t)-T_2(\infty)}{T(o)-T_2(\infty)}\right] = kt$$

The data for the 30% T_2 at P = 300 torr experiment are shown in Figure I-1. The line representing D_2 is slightly above the DT line, and the T_2 line is slightly below the DT line. This behavior is quite different from that observed by Pyper, et al [1], where there was a wide divergence between the three lines.

A set of experiments was done at P = 300 torr and T_2 = 30% to determine the reproducibility of k, the velocity constant [9]. In the third experiment, the D_2 was not mixed with the T_2 immediately following the introduction of the T_2 into the mixing cell because of a computer failure in the mass spectrometer system. The T_2 remained in the mixing chamber 24 hr before the D_2 was mixed in. The reaction time in this experiment was two and one-half times slower than in the first two experiments. The mean times, τ, for the

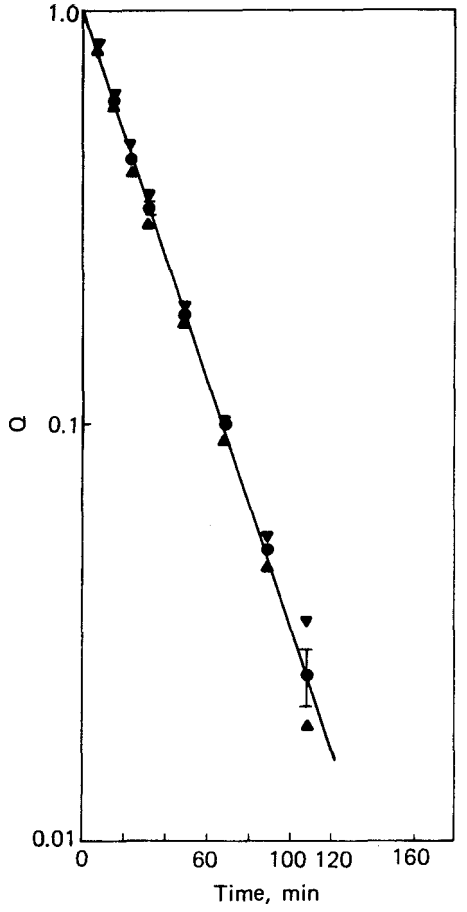

FIGURE I-1 - Reaction rate for 300 torr, 30% T_2 with components mixed at same time. ● growth of DT, ▼ decay of D_2, ▲ decay of T_2.

reaction to go to 1/e are given in Table I-1. It can be seen from the experiments at 300 torr that the reaction time dependence on the timing of the mixing of the gases is reproducible. Putting in the T_2 24 hr in advance reduced the reaction rate, whereas putting D_2 in 24 hr in advance increased the rates slightly. This behavior is shown in Figure I-2. It is also seen from the table that the same pattern appears at a pressure of P = 150 torr.

To learn why the change in reaction rate depended on the order in which the components were introduced into the mixing chamber, a second T_2 mass spectrometer sample

Table I-1 - REACTION TIMES FOR 30% T_2 EXPERIMENTS

Pressure (torr)	Condition	τ (min)
300	Mixed together	32
300	Mixed together, CT_4 60 ppm	36
300	T_2 in 24 hr	86
300	D_2 in 24 hr	29
300	T_2 in 24 hr, CT_4, 350 ppm	84
300	Mixed together	34
300	T_2 in 48 hr, CT_4, 530 ppm	105
150	Mixed together	47
150	T_2 in 24 hr	84
150	D_2 in 24 hr	39
40	Mixed together	125
20	Mixed together	280
20	T_2 in 24 hr	~500
500	Mixed together	34
300	T_2 in 24 hr, CT_4, 320 ppm	86
	Second T_2 Feed Gas - 120 ppm T_2O	
300	Mixed together	37
300	T_2 in 24 hr, CT_4, 380 ppm	94
300	T_2 in 12 hr, CT_4, 150 ppm	68
300	T_2 in 12 hr, CT_4, 150 ppm	59
300	T_2 in 12 hr, CT_4, 140 ppm	56

was taken just before mixing and a small amount of CT_4 (0.0035%) was detected in the sample. When the T_2 was mixed with 2.3 parts D_2, the CT_4 peak went below the detectable limit, explaining why the CT_4 or $CD_x T_{4-x}$ was not seen during the first experiment. A second experiment was done admitting the T_2 into the mixing chamber 48 hr in advance. As shown in Table I-1, the reaction time was slowed more, and 0.053% CT_4 was detected in the T_2 just before mixing.

The experiment with T_2 in the mixing cell 24 hr was repeated producing 0.032% CT_4. The initial T_2 was analyzed for impurities using a gas chromatograph, and the CT_4 content was found to be less than 25 ppm. The 29 and 32 min mean-time experiments are represented as having this amount of CT_4 in Figure I-3. The 36 min experiment had a trace of about 60 ppm CT_4. These points in Figure I-3 are represented by the filled circles.

Using a second batch of tritium T_2 [2], a point was measured at 150 $\pm$ 50 ppm CT_4 with a 69 min mean-time. The inlet pressure of the mass spectrometer was increased from 50 μm to 200 μm to reduce

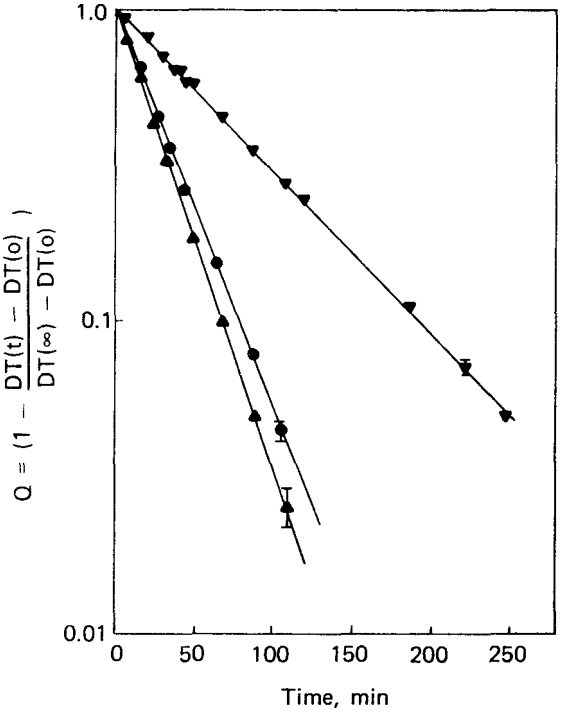

FIGURE I-2 - Growth of DT for 300 torr, 30% T_2 with mixtures made in different ways: ● mixed together, ▼ T_2 in cell 24 hr in advance of D_2, ▲ D_2 in container 24 hr in advance of T_2.

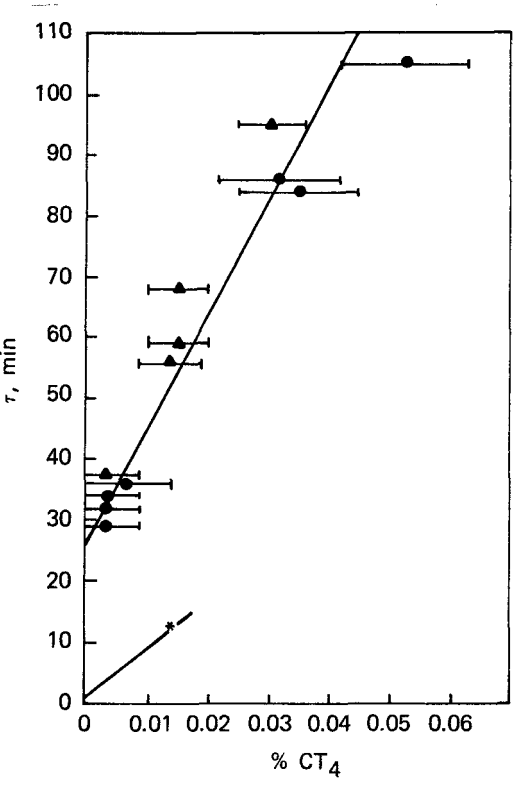

FIGURE I-3 - Effect of the presence of CT_4 in 30% T_2 mixture on the half-time for the reaction: ●samples contain only CT_4 impurity, ▲samples also contain 120 ppm T_2O, * represents a 90% T_2 sample (see text).

the uncertainty in the CT_4 determination. This point appears to be above the filled circles. A possible reason is that there was also about 120 ppm T_2O in this T_2 batch. All subsequent points in Figure I-3 using this T_2 batch are represented by triangles. They all fall above the closed circles of the first T_2 batch, but the error bars all overlap except for the 69 min point. Since it is very difficult to produce a water vapor mass spectrometer standard, the sensitivity of the spectrometer to T_2O is now known. The line in the figure represents all the points. Assuming that the T_2O and CT_4 sensitivities are about the same, one can add the two impurity concentrations, thus moving the triangles about 0.01% higher, and produce a much better fit to a line. However, as will be shown later, there is no basis for assuming that T_2O has any effect. Of the several measurements made with no detected impurities, the fact that none was faster than the 29 min mean-time indicates that the intercept of about 30 min is real for the 30% T_2 mixtures.

From the observed rate of production of CT_4 in the mixing cell, when T_2 is present in the 24 to 48 hr period, one would expect about 15 ppm/hr during an experiment. The change in slope of the ℓnQ as a function of t would be hard to observe except possibly in the long low pressure experiments.

The results in Table I-1 can be expressed in terms of the number of DT molecules produced per ion pair produced by the β^- from the tritium. Following Lind [10], the yield G is given by $G = (100/w)(M/N)$, where w is the energy to produce an ion pair, 36.6 eV [11], M the number of DT molecules produced in an initial unit time, and N [10] is the number of ion pairs formed in the gas. Thus, from Equation 1:

$$\frac{dDT}{dt}\Big|_o = kDT(\infty) = M \qquad (4)$$

$N = f\ I\ n\ g$, where I = 155, the average β^- energy divided by w [11], f is the fraction of the β^- energy deposited in the gas, n is the number of disintegrations per minute per gram of T_2, and g the number of grams of T_2. The quantities used in determining G in the cases where 30% T_2 was mixed with D_2 are shown in the first section of Table I-2. The second section of the table indicates the reduction in yield when CT_4 appears in the T_2 and is allowed to stand in the mixing chamber before adding the D_2. The 300 torr points also appear in Figure I-3.

The effect of varying the T_2 concentration is quite dramatic. The T_2 concentration was varied from 10 to 90% in three different impurity circumstances as shown in Table I-3 and Figures I-4 and I-5. When about 120 ppm CT_4 is in the T_2, the reaction rate, k, appears to be linear in T_2. Unfortunately, there was about 120 ppm T_2O in these experiments. The linear variation in k produces a yield which only depends on the final DT concentration producing a maximum at T_2 = 50%. In the second set of experiments, T_2 feed gas was used containing the T_2O and no detectable CT_4 (less than 30 to 40 ppm), and k appears to increase nearly exponentially for high T_2 concentration. There is a marked difference in CT_4 or T_2O effecting the results. We then obtained T_2 feed gas in which no CT_4 or T_2O was detectable, and the third set of experiments are shown in the third section of Table I-3. These results, as shown in Figures I-4 and I-5, are lower than with the T_2O present. The decrease in the yield at T_2 = 90% suggests the presence of undetected CT_4 impurity which will be addressed in the following discussion.

Table I-2 - DEPENDENCE OF REACTION RATE AND YIELD ON PRESSURE

P	T_2(gm)	f	N	k	DT(∞)	M	G
500	0.0158	1.0	5.32×10^{16}	0.0294	41%	6.39×10^{19}	3300
300	0.0095	1.0	3.19	0.0286	41	3.74	3190
150	0.0048	0.70	1.60	0.0212	41	1.39	3390
40	0.0013	0.22	0.43	0.0079	41	0.136	3990
20	0.00065	0.08	0.21	0.0036	41	0.030	4960
300	T_2, 24 hr advance		3.19×10^{16}	0.0118	41	1.54×10^{19}	1320
300	T_2, 48 hr advance		3.19	0.0095	41	1.24	1050
150	T_2, 24 hr advance		1.60	0.0120	41	0.78	2640
20	T_2, 24 hr advance		0.21	0.0058	41	0.017	2780

Table I-3 - DEPENDENCE OF REACTION RATE AND YIELD ON T_2 CONCENTRATION

P (torr)	T_2 (%)	N	k (min^{-1})	DT(∞) (%)	M	G
(1) Impurities; CT_4 - 130 ± ppm, T_2O - 120 ± 30 ppm						
300	30	3.19×10^{16}	0.0286	41.2	3.74×10^{19}	3190
300	50	5.13	0.0416	48.4	6.41	3400
300	75	7.97	0.0625	36.6	7.30	2510
300	91	9.68	0.0769	16.3	4.00	1130
(2) Impurities; CT_4 - <40 ppm, T_2O - 120 ± 30 ppm						
300	30	3.19×10^{16}	0.0270	41.2	3.55×10^{19}	3030
300	50	5.13	0.0555	48.6	8.61	4590
300	61	6.24	0.0909	45.8	13.29	5820
300	76	8.08	0.190	35.2	21.39	7230
300	91	9.68	0.66	15.3	31.07	8870
300	90	9.57	0.66	15.3	31.43	8970
(3) Impurities not detected <40 ppm						
300	10	1.06×10^{16}	0.0107	14.6	0.66×10^{19}	1800
300	30	3.19	0.0255	41.6	3.39	2900
300	60	6.14	0.0714	47.2	10.80	4780
300	74	7.86	0.143	36.8	16.76	5830
300	90	9.57	0.286	19.0	17.31	4980

DISCUSSION

We have made measurements of the rate of reaction of T_2 and D_2 mixtures in a specially prepared stainless steel container. Small amounts of CT_4 could be made to appear in the container by soaking the interior of it with T_2 for different lengths of time. No CT_4 appeared in the 2-liter Quantum Mechanics container where the T_2 for mixing experiments was stored for more than a month at a time. Thus, the methane most likely came from handling the platinum thermometer with oil-contaminated glovebox gloves when it was put into the mixing cell after calibration. This source gave us a convenient way of adding very small amounts of CT_4 to the T_2 that was to be mixed with D_2. Schaeffer and Thompson [6] showed that the radiation-induced reaction in H_2+D_2 mixtures was an ion-molecule chain reaction by adding Kr and Xe to their mixtures in small quantities. The addition of these inert gases greatly slowed the reactions by transferring the charge of the three body ion to the inert gas thus stopping the chain. The ionization potential for CT_4 of 13.1 eV is comparable to Kr. Thus, the dramatic slowing of the present reaction with CT_4 present is evidence that the ion-molecule reaction describes the reactions in the present stainless steel mixing cell.

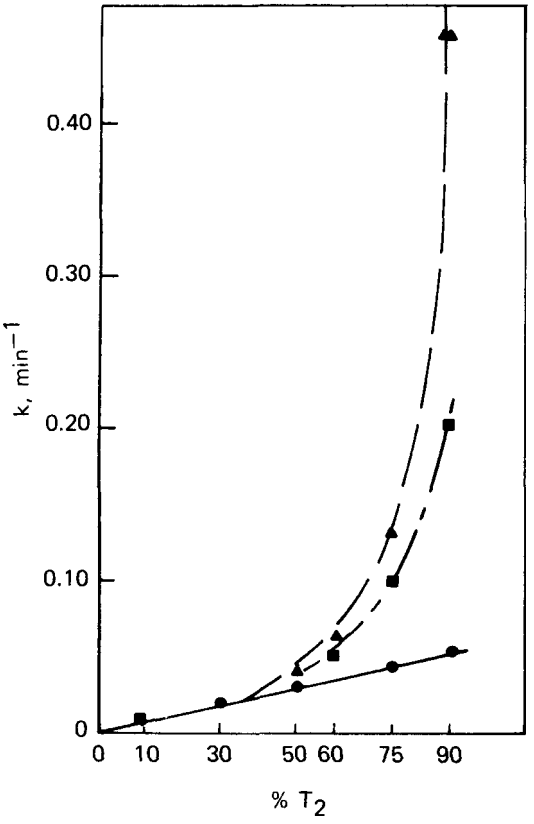

FIGURE I-4 - Reaction rate, k, as a function of T_2 concentration for the three cases in Table III: ● case 1, ▲ case 2, ■ case 3.

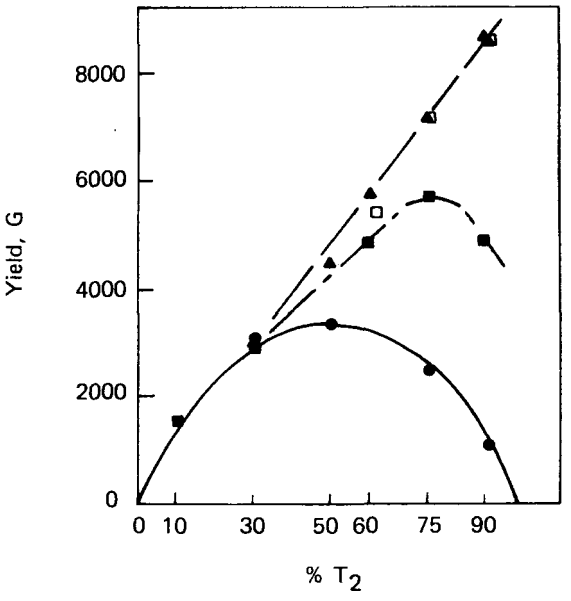

FIGURE I-5 - Yield G, as a function of T_2 concentration for the three cases in Table I-3. Symbols same as in Figure 4 plus □ representing case 3 after correction for CT_4 impurity (see text).

The reaction yields shown in the first part of Table I-2 indicates that G is nearly constant at the higher pressures with a slight increase at lower pressures. The increase in G is larger than the uncertainty in k for the 20 torr experiment, but there is no way of knowing whether the impurity content was smaller in the experiments with smaller T_2 content because of the lower total pressure. The presence of CT_4 clearly reduces the yield, even at low pressures. A gas phase reaction is indicated by the independence of yield on changing pressure.

As the CT_4 concentration goes to zero, the reaction rate as a function of T_2 concentration increases dramatically. Some of the experiments appear to be complicated by the presence of a second impurity, T_2O. We will show little or no effect on the reaction rate for T_2 concentrations greater than 50%. The 90% T_2 experiments can be used to put an upper limit on the CT_4 concentration in the cleanest experiments where the CT_4 was below the limit of detectability of mass spectrometer. In Figure I-3, the concentration dependence of the reaction rate with 30% T_2 samples on CT_4 is shown to be linear with an intercept of 30 minutes. If on the same figure one plots the 90% T_2 experiment with 130 ppm CT_4, the star (*) represents the 12 min τ for that experiment. The absolute lower limit for τ in the case of $CT_4 = 0$ is τ 0. The fastest 90% T_2

experiment with τ = 1.5 min could have been extremely free of CT_4 (<1 ppm) so it represents an upper limit on the τ axis. In the absence of other evidence we will take an intercept of half the difference. On the line represented by this intercept and τ = 12 minute at CT_4 - 130 ppm, 1.5 minute (k = 0.46) represents 8 ppm CT_4 and 3.5 minute (k = 0.198) represents 32 ppm.

Table I-3 and Figures I-4 and I-5 show that there is a large difference in the T_2 concentration dependence of the reaction rates when CT_4 and T_2O are present as impurities. A third set of experiments with neither T_2O nor CT_4 detectable in the T_2 produced values of k smaller than the experiments when only the T_2O was present for the same T_2 concentration. Assuming that the T_2 gas in section 2 of Table I-3 contained ∿8 ppm CT_4, then the τ = ln 2/k for entries in section 3 of Table I-3 correspond to CT_4 = 32 ppm. One then can use the later points along with the τ corresponding to CT_4 = 130 ppm for T_2 = 60% and 75% to construct lines like the 90% line in Figure I-6. From these lines one obtains a τ = 5.3 min for 75% T_2 and 10.7 min for 60% T_2. When the yield is calculated, the three squares in Figure I-5 become coincident with the triangles at T_2 = 60, 75, and 90%. This argument indicates that, if one corrects the experiments represented by the closed squares for the different CT_4 content than that represented by the triangles, the experiments containing ∿120 ppm T_2O and <40 ppm T_2O for the same T_2 concentration have the same reaction rate. We conclude

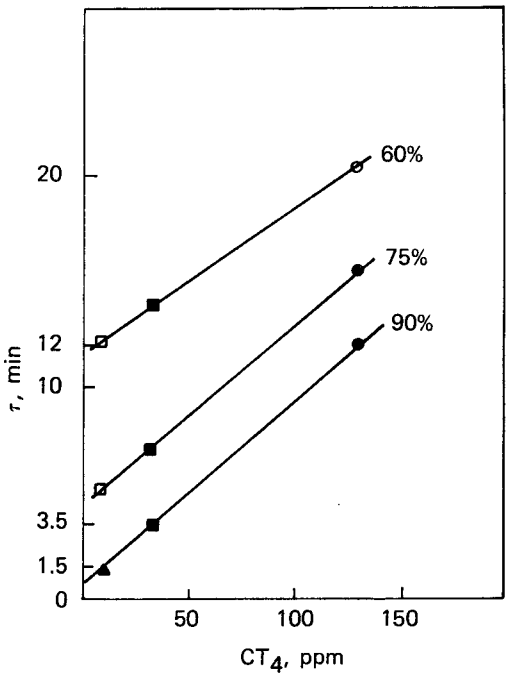

FIGURE I-6 - Construction using measured • half-times and concentrations (○ obtained from straight line in Figure I-4 for T_2 = 60%) to infer CT_4 concentrations for the measured half times, ●, ▲, ■. The open squares □ are corrected half-times.

that T_2O impurity of concentrations of the order of 100 ppm has no measurable effect on the reaction rate.

We are in the process of deriving a model for the shape of the curves in Figures I-4 and I-5. The very strong increase in k with T_2 (Figure I-4) in the clean material requires a large isotope effect. The large difference between the clean material and the 130 ppm CT_4 samples at T_2 = 90% indicates a large difference in the initial condition of the T_2. Tritium gas at room temperature is a complicated mixture containing T_2, T_2^* (excited states), T_2^+, T_3^+, T^-, and two kinds of electrons, fast electrons causing stripping reactions

and thermal electrons. We have done a model calculation [12] to determine the density of the charged species in T_2 and T_2 containing CT_4. The electrical conductivity measurements of T_2 by Souers, et al [11] indicate a negative ion to electron ratio of 100. Using the vibrational excited state cross section data of Allen and Wong [13], of the order of five T_2^* molecules in the fourth excited state per 10^5 T_2 can produce the T^- to electron ratio observed by Souers, et al. There is a very large isotope effect in the reaction $e^- + T_2^* \rightarrow T + T^-$, which can play a part in the increase in k in the increasing T_2 concentration. Our preliminary calculations indicate that the presence of $\sim$100 ppm CT_4 in T_2 can reduce the T_3^+ concentration more than an order of magnitude. We have yet to demonstrate that the presence of CT_4 reduces T_2^* in the model.

The data presented here, taken in a stainless steel system, has practical application in the handling of tritium mixtures. CT_4 is a very common impurity encountered in storing T_2 in metallic containers. These first data of reaction rates at high T_2 concentration present a rather complicated picture where excited state molecules play a definite role.

We have begun to study the temperature dependence of the reaction rate as a function of T_2 concentration. The experiments were done with the present mixing cell immersed in liquid N_2 for the 77 K points, in dry ice for the 195 K points, and a water-ice bath for the 273 K points. The results of these experiments in terms of the mean-time for the reaction are shown in Table I-4. In these experiments, the impurity level was <40 ppm. The results at 300, 273, and 77 K indicate a general slowing of the reaction rate with decreasing temperature. The rates at 195 K are extremely fast. For T_2 concentrations above 50%, the reaction was finished by the time the first mass spectrometer sample was taken 2 min after the start of mixing. At 77 K the dramatic increase in the rate with increasing T_2 concentration seems to have disappeared. The variation in the mean-time under the same conditions at 77 K indicates the reaction may be being controlled by undetected impurities.

Table I-4 TEMPERATURE DEPENDENCE OF τ (MIN)

$\%T_2/T(K)$	300	273	195	77
10	93		14	
30	32	39	1.8	140-180
50	18	19	<0.5	
60	14			
75	7	9.5	<0.5	
90	1.5	8.5	<0.5	220-280

The resonant like behavior at 195 K is being investigated with more experiments near 195 K. The fast mixing at this temperature offers a practical way of equilibrating mixtures with a dry ice cold finger in T_2 handling systems.

A calculation of charged particle densities in tritium gas

G. T. McConville

In a recent measurement of the electrical conductivity of T_2 gas, Souers, et al [11] found that the negative charge is carried predominately by negative ions in a ratio of 100 to 1 rather than by electrons. This ratio can be explained by the presence of T_2 molecules in excited vibrational states by assuming pure tritium gas to be made up of a mixture of the following species: T_2, T_2^*, T_2^+, T_3^+, T_5^+, T^-, and e^-. The electrons form three groups: β^- from the T_2 disintegrations; e_2^-, hot electrons; and e_3^-, thermal electrons. In the following we will consider β^- and e_2 to be the same with an average energy of 100 eV, and e_3 to have an evergy of 0.1 eV. T_2^* has an internal energy of about 2 eV.

The equations of interaction of these species and their reaction rates are given in Table I-5.

Assuming the T_2 is in a steady state, the following equations are formed:

$$\frac{dT_2^+}{dt} = ne_1^-(T_2)K_1 + (T_3^+)(e_3^-)K_5 - (e_3^-)(T_2^+)K_4 - (T_2)(T_2^+)K_2 = 0$$

$$\frac{de_3^-}{dt} = ne_1^-(T_2)K_1 - (e_3^-)(T_2^*)K_8 - (e_3^-)(T_2^+)K_4 - (e_3^-)(T_3^+)(K_4 + K_5) = 0 \qquad (5)$$

$$\frac{dT_3^+}{dt} = (T_2^+)(T_2)K_2 - (T_3^+)(T_2)K_2 - (T_3^+)[(e_3^-)(K_4 + K_5) + T^-K_6] = 0$$

$$\frac{dT^-}{dt} = (e_3^-)(T_2^*)K_8 + (e_3^-(T_2)K_5 - (T_3^+)(T^-)K_6 = 0.$$

Table I-5 - REACTION RATES [14] FOR EQUATIONS RELATING CHARGES SPECIES

Reaction	Rates cm^3/molecule sec	
$n(e_1^- + T_2 \rightarrow T_2^+ + 2e_3^-)$	5×10^{-9}	K_1
$e_3^- + T_2 \rightarrow T + T^-$	1×10^{-14}	K_3
$e_3^- + T_2^* \rightarrow T + T^-$	1×10^{-9}	K_3
$T_2^+ + T_2 \rightarrow T_3^+ + T$	1.0×10^{-9}	K_2
$T_3^+ + e^- \rightarrow T_2 + T$	5×10^{-9}	K_4
$T_3^+ + e^- \rightarrow T_2 + T^-$	1.8×10^{-8}	K_5
$T_3^+ + T^- \rightarrow 2T_2$	5×10^{-8}	K_6
$T + T + M = T_2 + M$	3×10^{0}	K_7

In the solution of these equations, (T_2) is large and can be considered a constant, which is 10^{21} for the present mixing chamber. One has to make an independent estimate of (e_1^-). Assuming 2×10^{15} dis/mole sec for T_2, the mixing chamber containing 1.6×10^{-3} moles produces one e_1 every 3×10^{-13} sec. The e_1 makes n = 155 ionizing collisions losing 36.6 eV per collision. The average path length of the e_1^- is 0.26 cm, so most of the collisions are nonionizing. About 16 eV is lost in these inelastic collisions for every ionizing collision. The lifetime of the e_1^- is about 2.5×10^{-9} sec before it becomes e_3^-. Thus, in the steady state at any time $(e_1^-) = 8 \times 10^3$ in the mixing chamber. From the above equations:

$$T_2^+ = \frac{ne_1(T_2)K_2 + (T_3^+)(e_3^-)K_5}{(e_3^-)K_4 + (T_2)K_2} \quad (6)$$

$$T_3^+ = \frac{(T_2^+)(T_2)K_2}{e_3^-(K_4 + K_5) + T^-K_6} \quad (7)$$

$$e_3^- = \frac{ne_1(T_2)K_1}{(T_2^*)K_8 + T_2^+K_4 + T_3^+(K_4 + K_5)} \quad (8)$$

$$T^- = \frac{(e_3^-)(T_2^*)K_8 + (T_3^+)(e_3^-)K_5}{T_3^+ + K_6} \quad (9)$$

From the reaction table, one can see that $e_3^- + T_2$, when T_2 is in the ground state, has a very small cross section for reaction. Allan and Wong [13] have observed that the cross section increases orders of magnitude when H_2 or D_2 is in excited vibrational states. The increase for D_2 is greater than for H_2. One would expect the increase to be even greater for T_2. On that basis, we take T_2^* to represent one excited state of $\nu = 4$ with an internal energy of about 1 eV for a model calculation of the concentrations of T_2^+, T_3^+, T^- and e_3^- in T_2 gas. Thus, $K_8 = 1 \times 10^{-9}$ cm^3/molecule sec represents the rate for this particular T_2^*.

As a starting point in the model calculation, we assume $T_2^+ << T_3^+$ (which turns out to be true) and $T_2^* \sim 0$. Then from Equation 8:

$$(e_3^-)(T_3^+) = ne_1^-(T_2)\frac{K_1}{K_4+K_5} = 3.2 \times 10^{26} \quad (10)$$

Thus, for $(T_2) = 10^{21}$ and (T^-) assumed small $(e_3^-) = (T_3^+) = 1.6 \times 10^{13}$. Then from Equation 9, $T^- = e_3^-K_5/K_6 = 6 \times 10^{12}$. Now $e_3^-K_5/K_6 = 6 \times 10^{12}$. Now $e_3^- + T^-$ has to equal T_3^+ at room temperature since T_5^+ is small. Iterating between Equations 6, 8, and 9, we arrive at a consistent set of $(e_3^-) = 1.6 \times 10^{13}$, $(T^-) = 5.0 \times 10^{12}$. and $(T_3^+) = 2.0 \times 10^{13}$. Considering the precision of the reaction rates in Table I-5, the above consistency is reasonable. From Equation 6, $T_2^+ = 9 \times 10^7$ which is much smaller than T_3^+.

In Souer's electrical conductivity experiment [11], it was found $(e_3^-) << (T^-)$, and he proposed $e^- + T \rightarrow T^-$ as the producing reaction. This reaction has a cross section of the order of 10^{-20} cm^2 which produces a rate of the order of K_3 in Table I-6. We will show that increasing T_2^* produces T^- at the expense of e_3^-. The effect of increasing T_2^* and determining T_2^+, T_3^+, T^-, and e_3^- iteratively from Equations 6 through 9 is shown is Table I-7.

Table I-6 - VARIATION OF CHARGED SPECIES AS A FUNCTION OF EXCITED STATE T_2 MOLECULE NUMBER

T_2^*	T_2^+	T_3^+	e_3^-	T^-
0	1.9×10^7	2.0×10^{13}	1.6×10^{13}	5.0×10^{12}
10^{15}	7.1×10^6	1.3×10^{13}	4.7×10^{13}	9.1×10^{12}
10^{16}	6.1×10^6	1.1×10^{13}	5.8×10^{12}	1.1×10^{13}
10^{16}	6.0×10^6	1.1×10^{13}	6.0×10^{11}	1.1×10^{13}

Table I-7 - COMPARISON OF T_2 GAS AND H_2 PLASMA

	T_2 p = 1 atm	H_2 plasma
M_2	2.7×10^{19}/cc	4×10^{14}/cc
e_{hot}	2.1×10^2	2×10^7
e_3^-	5.6×10^9	2×10^{10}
M^-	3.0×10^{11}	4×10^9
M_2^+	1.6×10^5	1.2×10^9
M_3^+	3.0×10^{11}	2.2×10^{10}
M_2^*	1.3×10^{15}	?

From this model calculation a ratio of T^-/e_3^- of about 100 indicates an excited state T_2 concentration of $T_2^* \sim 5 \times 10^{16}$ or 5 parts in 10^5 of the ground state T_2.

In a real case rather than the single level model, the internal energy would be distributed in the first four or five vibrational levels. The number of species per cm^3 is given in Table I-7 for the calculated case of $T^-/e_3^- \approx 100$ where they are compared to a H_2 plasma [15] where the hot particles are 120 eV electrons.

Comparison of the ratios of M_2^+/M_3^+ and e_3^-/M^- in the two cases shows that the difference is loss mechanisms in the two cases; internal energy in the T_2 gas and the container walls in the plasma play a large part in the distribution of charges among the species in the mixture.

Low temperature trennschaukel

D. Cain and W. L. Taylor

The modified low temperature trennschaukel (described in detail in a previous report) [16] is being used to study the temperature dependence of the thermal diffusion factor, α_T, of equimolar ^4He-^{20}Ne mixtures. To date, experiments have been performed at 82 and 100 K (average temperature), and preparations are being made for experiments near 30 K. Temperature control has been within a few hundredths of a Kelvin of setpoint or less - an order of magnitude better than anticipated. The in situ thermal conductivity gas analyzing bridges have been stable, reproducible, and more sensitive to gas composition changes than mass spectroscopy. The experiments have yielded thermal diffusion factors in good agreement with theoretical calculations.

The major portion of the work involved in running these experiments is in the calibration of the thermistor thermal conductivity gas analyzing bridges. This is accomplished by controlling the apparatus at experimental conditions, filling the apparatus with mixtures of known composition which span the composition range of interest, and recording the bridge imbalance. This generates a curve of gas composition as a function of bridge output (bridge imbalance). When running an experiment, the gas mixture composition in several parts of the apparatus may be determined at any time by setting up the appropriate bridge, reading the bridge output, and comparing this with the calibration curve. Mixtures of precisely known composition were prepared in the Mound analytical section [17] for the calibrations; they are of nominal composition (mole fraction) 0.45 ^{4}He/0.55 ^{20}Ne, 0.50 ^{4}He/0.50 ^{20}Ne, and 0.55 ^{4}He/0.45 ^{20}Ne.

The first step in the calibration procedure is to determine the hot and cold temperatures, equally spaced about the average temperature of interest, at which the top and bottom sections, respectively, of the trennschaukel are to be controlled. The temperature difference must not be so large that the separation achieved in the 10-tube trennschaukel exceeds the range spanned by the calibration mixtures.

Once the temperatures have been determined, the entire device is evacuated and its temperature controlled at the temperature that the bottom (cold) section will assume during an experiment. The reference cells are purged and re-evacuated with the 0.50 He/0.50 Ne mixture; the two-bulb and trennschaukel parts of the apparatus are then purged and re-evacuated with the calibration mixture of interest. The reference cells are then filled with the 0.50 He/0.50 Ne mixture to the pressure that will be used during the experiment; the trennschaukel and two-bulb sections are filled to the same pressure with the calibration mixture. Wheatstone bridges are then wired using two fixed resistors, the thermistor in the bottom (cold) reference cell, and, in turn, the thermistor in each bottom (cold) location of the trennschaukel (or two-bulb). The bridges are biased with a stable DC voltage, allowed to stabilize, and the output voltage (bridge imbalance) for each bridge recorded.

The temperature of the entire apparatus is then raised to the temperature that the top (hot) section will assume during an experiment. The pressures (which have increased with the increase in temperature at constant volume) are readjusted to that of the experiment. Bridges are set up between the top (hot) reference cell thermistor, the fixed resistors, and the various sensing thermistors in the top section of the apparatus.

The entire device is then pumped out overnight, and the process is repeated with another calibration mixture. The entire device must be controlled at a single temperature during calibration (even though it will be operated during an experiment with a temperature difference) to ensure that the concentration of the calibration mixture remains unchanged (and therefore, known); otherwise, a temperature difference would cause a change in composition by means of thermal diffusion. The purging of the device with the appropriate mixtures and subsequent re-evacuation before filling for calibration has proven to be necessary to get

reproducible calibration curves. This is not surprising since the trennschaukel represents a large volume at low temperature, being pumped out through small diameter capillary lines. Some residual gas from the previous calibration remains in the trennschaukel and alters the composition of the incoming gas unless the system is purged.

The compositions of the calibration mixtures are fitted to a quadratic function in the output voltages, V_o, to generate a calibration curve over the entire range of mixture compositions. That is, the constants, a, b, and c are determined by a least squares treatment for the equation $\chi_{He} = a\ V_o^2 + b\ V_o + c$, where χ_{He} is the mole fraction of ^4He in the calibration mixtures. Once the responses of the thermistor bridges to mixture composition under the experimental conditions have been ascertained, one can determine the composition in the various parts of the apparatus at any time during an experiment by setting up the appropriate bridge and reading the bridge output.

As mentioned above, thermal diffusion factors have been measured at average temperatures of 82 and 100 K. Figure I-7 shows both measured [18-22] and calculated [23-27] thermal diffusion factors, α_T, below 200K. The present data are shown as closed circles (●) for α_T measured in the trennschaukel and closed triangles (▲) for α_T measured in the two-bulb. There are two features shown in this figure which are worthy of note. The first is that the data taken in the trennschaukel agree with calculated values of α_T and that the data point shown for the two-bulb measurement does not. Operating conditions for these experiments were chosen so as to be favorable to trennschaukel measurements. Under these conditions, the separations in the two-bulb are small enough to be within the uncertainty of the two-bulb thermistor bridge calibrations; favorable conditions for two-bulb operation would utilize larger temperature differences. In other words, the trennschaukel and two-bulb operating conditions are not compatible. Two-bulb experiments have been suspended until after experiments are completed with the trennschaukel. The second important feature depicted in Figure I-7 involves the temperatures at which other workers have data.

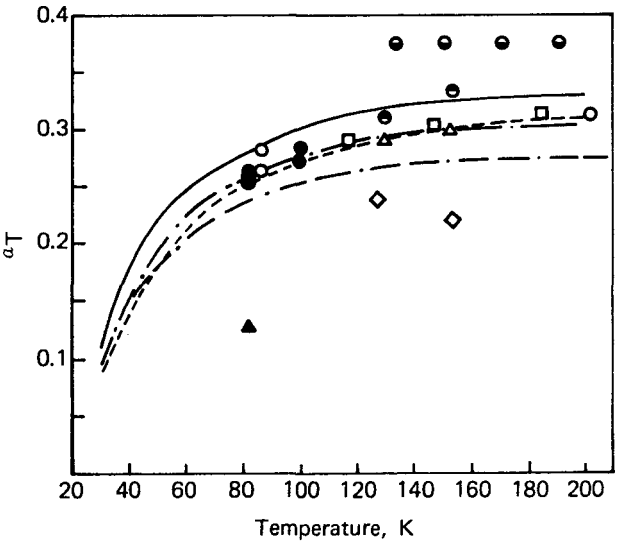

FIGURE I-7 - Temperature dependence of the thermal diffusion factor for equimolar He-Ne. The experimental points are: ●, present data (trennschaukel); ▲, present data (two bulb); ◒, Ibbs and Grew [18]; ◓, de Troyer, et al [19]; □, Grew [20]; △, van Itterbeek and de Troyer [21]; ◇, van Itterbeek, et al [22]; ○, Mound unpublished data. The curves are values of the thermal diffusion factor calculated from the following intermolecular potentials: – – ·, Dymond-Alder [23] with parameters given by Lin and Robinson [24]; ---, HFD [25]; ——, ESMSV [26]; —·—·, Exp-6 [27].

The open circles in the figure represent some badly scattered and unpublished data taken at Mound in a 7-tube trennschaukel. Excluding these, there are no published data for this system below 117 K. Thus, the present data extend into a temperature regime untested by other experimenters.

As stated previously, preparations are currently underway for experiments to be performed near 30 K. Plans are for further experiments extending up into the temperature range where other workers have data. The results of these experiments, as well as more detailed descriptions of the operating procedures and system performance, will appear in a future report.

II. Separation research

Liquid phase thermal diffusion

W. M. Rutherford

VISCOSITY OF METHYL CHLORIDE

The coefficients appearing in the theory of the thermal diffusion column are functions of the density, viscosity, diffusion coefficient, and thermal conductivity of the working fluid. Accurate values of these parameters as functions of temperature are required for theoretically predicting column performance and for interpreting experimental separation results in terms of the phenomenological theory of the thermal diffusion column. Good physical property data are especially important to the process of extracting information about the thermal diffusion factor from results of separation measurements.

Isotopic separation experiments with methyl chloride have been described in previous reports. In the process of evaluating the methyl chloride data, we found serious conflicts among the results of several sets of viscosity measurements published for liquid phase methyl chloride. Much of the data seemed unreasonable with respect to usually reliable correlation methods and with respect to the behavior of the other chlorinated methanes. The resulting uncertainty in the thermal diffusion factor derived from our experiments amounted to nearly a factor of two.

In a previous report [1] we described the construction and testing of a high pressure capillary viscometer designed to span the ranges of temperature and pressure typical of the working space of our experimental columns; i.e., 20 to 150°C and 1 to 100 atm. The apparatus is a steady flow capillary device similar in concept to those used by Flynn, Hanks, Lemaire, and Ross [2], by Kao, Ruska, and Kobayashi [3], and by Sun and Storvick [4]. The capillary is a 141.78 mm length of fused silica tubing with a nominal i.d. of 0.2 mm. Flow through the capillary is established by the movement of two identical piston syringes driven by a synchronous motor through an adjustable gear train. Water jackets on the syringes maintain the syringe temperatures at 25 $\pm$ 0.1°C. Pressure differential across the capillary is measured by a Sensotec wet/wet differential pressure transducer with a full-scale range of 0.5 psid and a nominal accuracy of $\pm$ 0.5% of full scale.

The modified Poiseuille equation for the viscosity in terms of the experimental parameters is:

$$\eta = \eta_p - mX \qquad (1)$$

where

$$\eta_p = \frac{\pi a^4 \Delta p}{8Q L_{eff}}$$

$$X = \frac{\rho Q}{8\pi L_{eff}}$$

$$Q = \frac{Q_o \rho_o}{\rho}$$

where

a = capillary radius
Δp = pressure difference across capillary
m = Hagenbach factor
Q = volumetric flow rate in the capillary

Q_o = volumetric flow rate at the pump temperature

L_{eff} = effective length of capillary

ρ = density of fluid in the capillary, and

ρ_o = density of fluid at the pump temperature.

The slip correction, the Couette correction, and the thermal expansion of the capillary are negligible for the conditions of the experiments. A value of 1.18 was assumed for the Hagenbach correction factor in keeping with results reported in references 2 and 4.

In a previous report [1], we described calibration and testing of apparatus with helium and nitrogen and reported some preliminary results for liquid phase methyl chloride. The following viscometer constant was derived from the helium data:

$$a^4/L_{eff} = 7.567 \pm 0.010 \times 10^{-10}$$

The measurements with nitrogen indicated that the overall precision of the apparatus was well within 1%.

The data for methyl chloride have now been extended to 69 and 103 atm and to 120 and 150°C.

Results of the measurements along with the results obtained previously are given in Table II-1. As in the previous work, measurements were made at two flow rates. Results at the two flow rates did not differ significantly except at 150°C, in the critical region. The corrected viscosities at 69 and 103 atm show a significant trend toward lower values at lower flow rates. This trend suggests incomplete temperature equilibration at the capillary entrance. Accordingly, the two sets of data were extrapolated to zero flow. These values are also given in Table II-1. It should be noted, however, that as the result of proximity to critical conditions (143.1°C and 65.9 atm) differential pressure fluctuations were rather severe during the measurements; thus, the experimental uncertainty at 69 atm and 150°C is estimated to be $\pm$ 5% and at 103 atm and 105°C, $\pm$ 3%.

Results are plotted as a function of density in Figure II-1. The data exhibit a typically smooth dependence on density, and they seem to be consistent with published low pressure gas measurements in the range of 0.01 to 0.015 cP.

The data in Figure II-1 were used to construct a table of viscosity values at saturation conditions. These results constitute Table II-2.

Figure II-2 is a plot of viscosity at saturation conditions as a function of temperature for this investigation and for the data available in the literature. Our data agree reasonably well with the very old data of de Haas [5] but fall substantially below the results of Stakelbeck [6], Benning and Markwood [7], and Awbery and Griffiths [8].

ISOTOPIC THERMAL DIFFUSION OF BROMOTRIFLUOROMETHANE

Bromotrifluoromethane was evaluated as a potential working fluid for the separation of bromine isotopes. In recent experiments we have used bromobenzene for this purpose; however, bromobenzene is relatively unsatisfactory because its high viscosity and small diffusion coefficient contribute to

Table II-1 - MEASUREMENTS OF THE VISCOSITY OF METHYL CHLORIDE

Temperature (°C)	Pressure (atm)	Q_o (cm^3/hr)	η_p (cP)	1.18 X (cP)	η
20	35.0	12.051	0.1871	0.00094	0.1861
		6.026	0.1871	0.00047	0.1866
40	35.0	12.051	0.1571	0.00094	0.1562
		6.026	0.1560	0.00047	0.1555
60	35.0	24.10	0.1317	0.00187	0.1298
		12.051	0.1302	0.00094	0.1293
90	35.0	24.10	0.1002	0.00187	0.09831
		12.051	0.09897	0.00094	0.09803
	69.0	24.10	0.1069	0.0019	0.1050
		12.051	0.1062	0.0009	0.1053
120	69.0	24.10	0.07767	0.00187	0.07580
		12.051	0.07682	0.00094	0.07588
	103.0	24.10	0.08611	0.00187	0.08424
		12.051	0.08444	0.00094	0.08351
150	69.0	24.10	0.25000	0.00187	0.02313
		12.051	0.02292	0.00094	0.02198
					0.02083[a]
	103.0	24.10	0.06171	0.00187	0.05983
		12.051	0.05973	0.00094	0.05879
		12.051	0.05937	0.00094	0.05844
					0.05740[a]

[a] extrapolated to $Q_o = 0$

Table II-2 - VISCOSITY OF SATURATED METHYL CHLORIDE

Temperature (°C)	Viscosity (cP)
20	0.1863
40	0.1513
60	0.1255
80	0.1057
100	0.0867
120	0.0670
130	0.0570
140	0.0451
143.1	0.0310

a relatively low isotopic transport rate. Other low molecular weight bromine compounds react with the hot walls of the columns forming undesirable corrosion products. Methyl bromide may be satisfactory, but it is a highly toxic compound, and we have sought to avoid using it.

Bromotrifluoromethane is a promosing candidate because it is chemically stable, it has a low viscosity, and it is relatively free of interference from ^{13}C. The major disadvantage to bromotrifluoromethane, however, is its extremely low critical

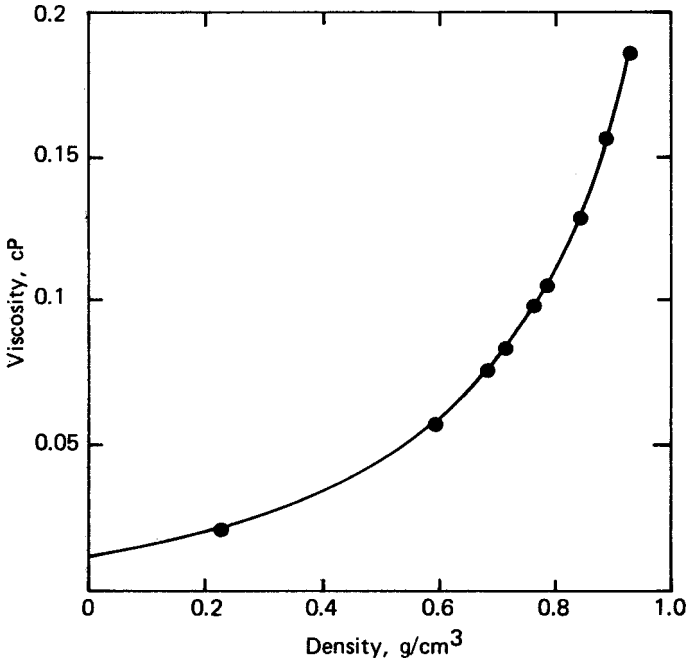

FIGURE II-1 - Viscosity of methyl chloride as a function of density.

temperature (67°C). Inasmuch as this temperature is significantly lower than typical hot wall temperatures, the column must be operated at pressures considerably in excess of the critical pressure of 39 atm.

The 45 cm research column was used for two separation experiments with bromotrifluoromethane. The separation of the ^{79}Br species from the ^{81}Br species was measured with the hot wall condensing steam supply at 6.8 atm (164°C) and at 2 atm (121°C). Conditions of the experiments are given in Table II-3 and the resulting separation factors are reported in Table II-4.

A small isotopic separation was observed in both instances. The effect is much too small for practical application in

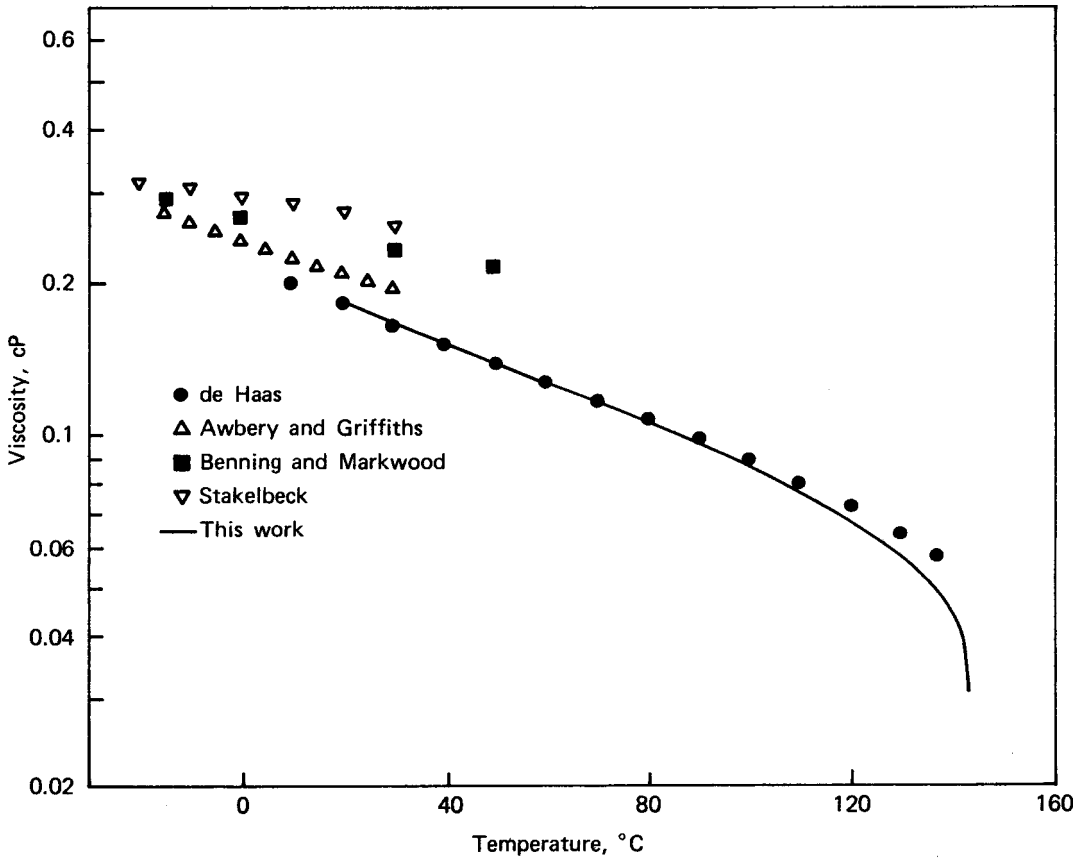

FIGURE II-2 - Viscosity of saturated liquid phase methyl chloride.

Table II-3 - DIMENSIONS AND OPERATING CONDITIONS FOR THERMAL DIFFUSION SEPARATION OF ISOTOPICALLY-SUBSTITUTED BROMOTRIFLUOROMETHANE

Column Length	45.6 cm
Hot Wall Diameter	1.8778 cm
Cold Wall Diameter	1.9286 cm
Steam Temperature	
Experiment 1	164°C
Experiment 2	121°C
Cooling Water Temperature	15°C
Heat Input	
Experiment 1	1235 W
Experiment 2	706 W
Pressure	123 atm

Table II-4 - THERMAL DIFFUSION SEPARATION OF ISOTOPICALLY-SUBSTITUTED BROMOTRIFLUOROMETHANE

	Time (hr)	Separation Factor
Experiment 1	24	1.050
	48	1.053
	72	1.064
	151	1.068
	192	1.064
	216	1.055
	240	1.068
Experiment 2	1	1.042
	3	1.043
	24	1.043

our 13-column experimental cascade. The effect is also too small to permit a useful assessment of the initial transport coefficient; however, the physical properties of the fluid suggest that this parameter might be relatively large.

BROMINE-79 SEPARATION

In a previous report [9] we discussed the beginning of an experimental campaign to separate ^{79}Br by liquid phase thermal diffusion of bromobenzene. The 13-column experimental cascade was operated in the batch mode with a 740 g feed reservoir at the bottom and a 16 g product reservoir at the top. After 64 days, when the top concentration had reached 70% ^{79}Br, the cascade was rearranged from a strictly series arrangement to a series-parallel configuration in order to accelerate the rate of transport of ^{79}Br. Progress of the separation is depicted in Figure II-3. After 149 days of operation, the first batch of product was removed at a ^{79}Br concentration of 90.3%. Periodic product withdrawals were sustained thereafter for a period of 205 days during which time some 88 g of ^{79}Br was accumulated for an average production rate of 0.43 g/day. The average enrichment was 90.6%.

Calcium isotope separation

W. M. Rutherford

Previous reports have described a process for separating calcium isotopes by liquid

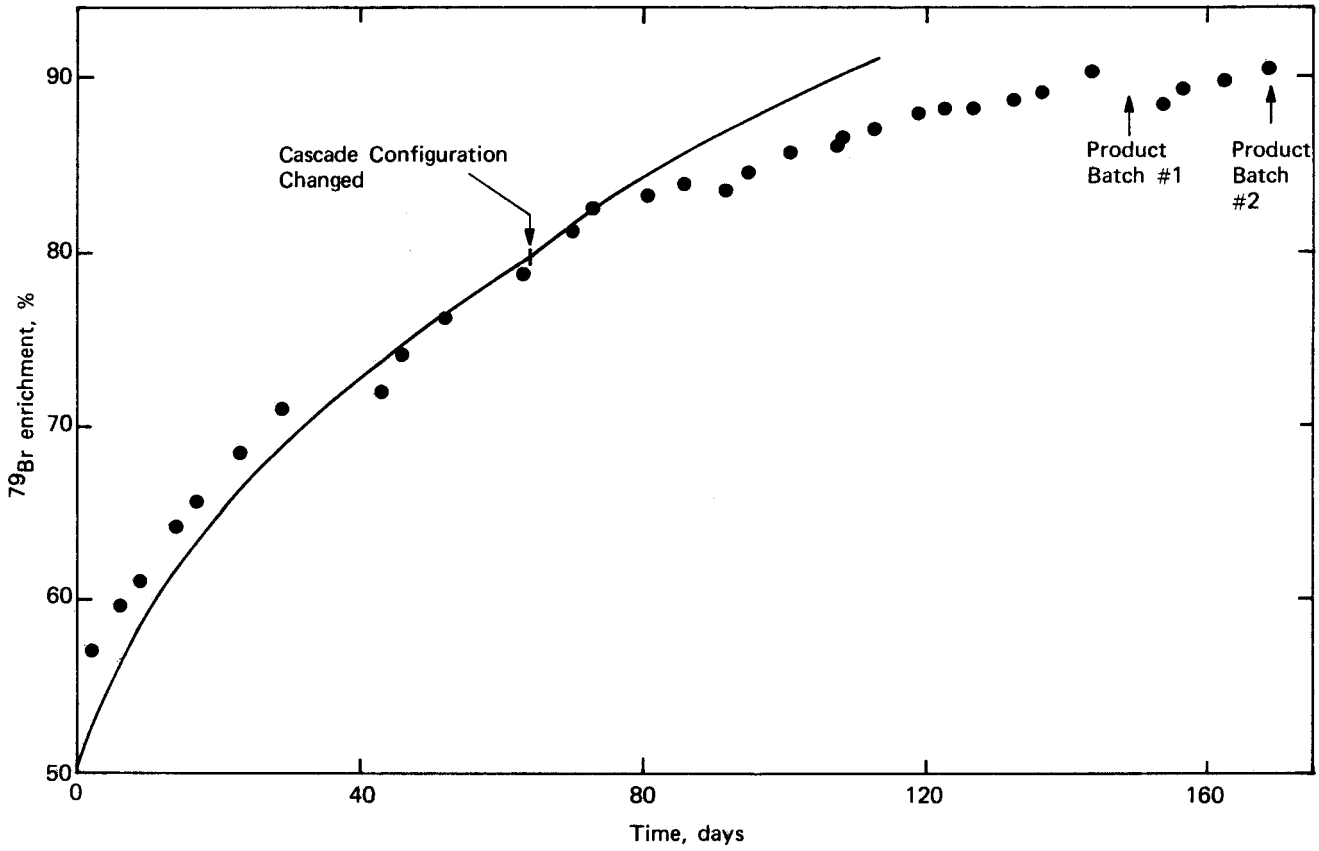

FIGURE II-3 - Separation of ^{79}Br by thermal diffusion of bromobenzene in the 13-column experimental cascade. The solid line is calculated from theory.

phase thermal diffusion of calcium compounds in solution [10]. A concept has been developed wherein the separation of the calcium salt from the solution is suppressed by setting up a net flow of solvent through the apparatus at a rate just sufficient to offset the solute-solvent separation. Most of the experiments have been carried out with $Ca(NO_3)_2$ in water; however, heavy water has also been used as a solvent, and systems involving calcium trifluoroacetate in alcohol solvents have been evaluated. There appears to be no significant advantage to alternative systems; therefore, current work is directed almost entirely toward full evaluation and optimization of the aqueous $Ca(NO_3)_2$ system.

The experiments with $Ca(NO_3)_2$ have three objectives. These are: 1) to determine the initial transport rate for the solute-solvent pair in order to establish the criterion for setting the solvent counterflow rate, 2) to determine the steady state separation of the ^{40}Ca - ^{48}Ca pair, and 3) to determine the initial transport rate of the ^{48}Ca isotope.

Two complete systems are being used for the calcium isotope separation experiments. The first system, constructed around a 114 cm liquid phase thermal diffusion column, was described in a previous report [11]. A second counterflow apparatus based on a 15 cm thermal diffusion column was assembled in order to accelerate the rate at which data can be accumulated [12].

Both counterflow systems are similar in principle; however, the long column is now fully automated. Density of the solution at the bottom of the column is monitored continuously by means of a Mettler-Paar digital density meter, the output of which is processed by an ADAC computer system to generate a control signal for establishing the solvent injection rate. The short column is inherently easier to control, and so far it has been successfully operated manually.

During this reporting period, four experiments were run with the 114 cm column and two with the 15 cm column. An additional, unsuccessful attempt was made to induce a separation in the short column for the calcium trifluoroacetate-ethanol system.

Two of the four long column experiments and one of two short column experiments have been completed successfully without control or equipment failures. Starting solute concentrations for these runs range from 4.1 to 37 wt. % $Ca(NO_3)_2$ in water. Solute concentrations were measured during the startup phase of the experiments while the desired working solute concentration difference was being established between the top and bottom reservoirs of the column. These data were used to determine the initial transport coefficient for the solute-solvent separation.

According to the theory of the thermal diffusion column, the inital rate at which solute is accumulated in the bottom of the column is given by:

$$(dm_2/dt)_{t=o} = H_{ss} w_1 w_2 \qquad (1)$$

where we have assumed that the reservoir at the bottom of the column is large in comparison to the holdup in the column, and where H_{ss} is the initial transport coefficient for the solute-solvent pair, m_2 is the mass of solute in the bottom reservoir, and w_1 and w_2 are the mass fractions of solvent and solute, respectively. The quantity dm_2/dt is derived from dw_2/dt, the initial rate of change of the composition at the bottom of the column before solvent injection is started. Thus,

$$dm_2/dt = V[\rho + w_2 (\frac{dp}{dw_2})]dw_2/dt \qquad (2)$$

where V is the reservoir volume and ρ is the density.

The resulting transport coefficients are reported in Table II-5. According to the theory of the solvent counterflow apparatus, the solute-solvent concentration gradient in the column is reduced to zero when:

$$\sigma = H_{ss} w_1 \qquad (3)$$

where σ is the solvent injection rate. Values of σ calculated from Equation 3 are given in Table II-5 and plotted in Figure II-4.

Table II-5 - TRANSPORT DATA FOR LIQUID PHASE THERMAL DIFFUSION OF THE $Ca(NO_3)_2$ - WATER SYSTEM

Column Length (cm)	w_2 (%) (top reservoir)	$10^5 H_{ss}$ (g/sec)	σ (g/hr) (Eq. 3)
114	4.85	21.8	0.748
114	24.95	13.9	0.375
15	5.04	23.0	0.793
15	38	11.3	0.257

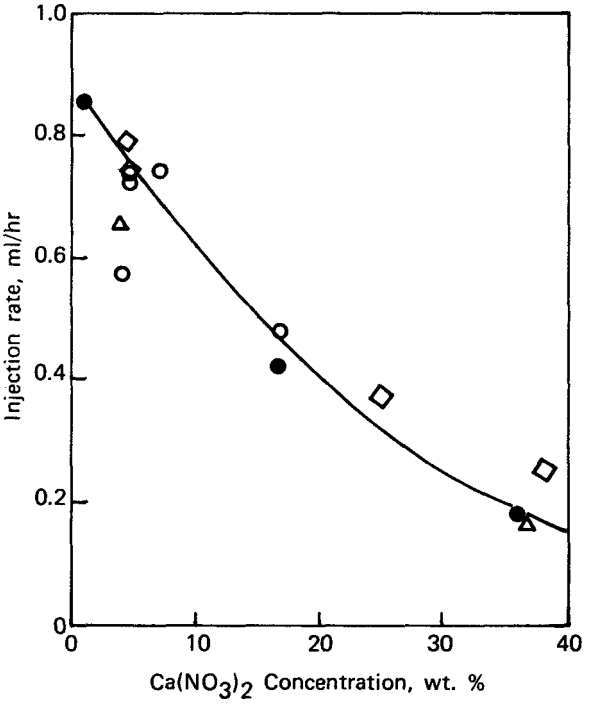

FIGURE II-4 - Solvent injection rate for the $Ca(NO_3)_2$ - water system. The symbols are as follows: 70 cm column, ●; 114 cm column, ○; 15 cm column, △; calculated from Equation 3, ◇.

Figure II-4 is also a plot of the experimental injection rate as a function of concentration for all of the experiments run so far, including earlier data from a 70 cm column. The experimental injection rate is adjusted so as to create a stable concentration difference of 3 to 8 wt. % in the solute concentrations between the top and bottom ends of the column. (The concomitant density gradient stabilizes the column against undesired parasitic fluid circulation). The experimental rates, therefore, do not strictly represent the zero-gradient condition of Equation 3, but the difference should be small.

The isotopic separations as functions of time are plotted for three of the experiments in Figures II-5, II-6, and II-7. The quantities plotted are the ratios of ^{48}Ca to ^{40}Ca in the top and bottom reservoirs of the column. Equilibrium separation factors for the ^{48}Ca - ^{40}Ca pair are given in Table II-6. The separation factor q is defined by:

$$q = \frac{(w_{48}/w_{40})_{bottom}}{(w_{48}/w_{40})_{top}} \qquad (4)$$

where w_{48} and w_{40} are the mass fractions of ^{48}Ca and ^{40}Ca, respectively.

Exponential curves were fitted to the time dependent isotopic concentration data in order to determine the initial rate of transport of ^{48}Ca. Thus, the initial rate of increase in the ^{48}Ca concentration is given by:

$$(dw_{48}/dt)_{t=o} = C/t_r \qquad (5)$$

where C and t_r are the constants of the exponential curve fitted to the data for the data for the bottom reservoir of the column, and w_{48} is mass fraction ^{48}Ca in total calcium. The rate of transport of ^{48}Ca is then given by:

$$\frac{dm_{48}}{dt} = \frac{40.08}{164.09} \; w_2 V\rho \; \frac{dw_{48}}{dt} \qquad (6)$$

where m_{48} is the mass of ^{48}Ca in the reservoir, w_2 is the mass fraction of $Ca(NO_3)_2$ in the reservoir, V is the volume of the reservoir, and ρ is the density of the solution.

The resulting transport rates, which are quite low, are given in Table II-6. At this time the meaning of these results, with respect to predicting the probable size and configuration of apparatus for practical scale separations, is uncertain.

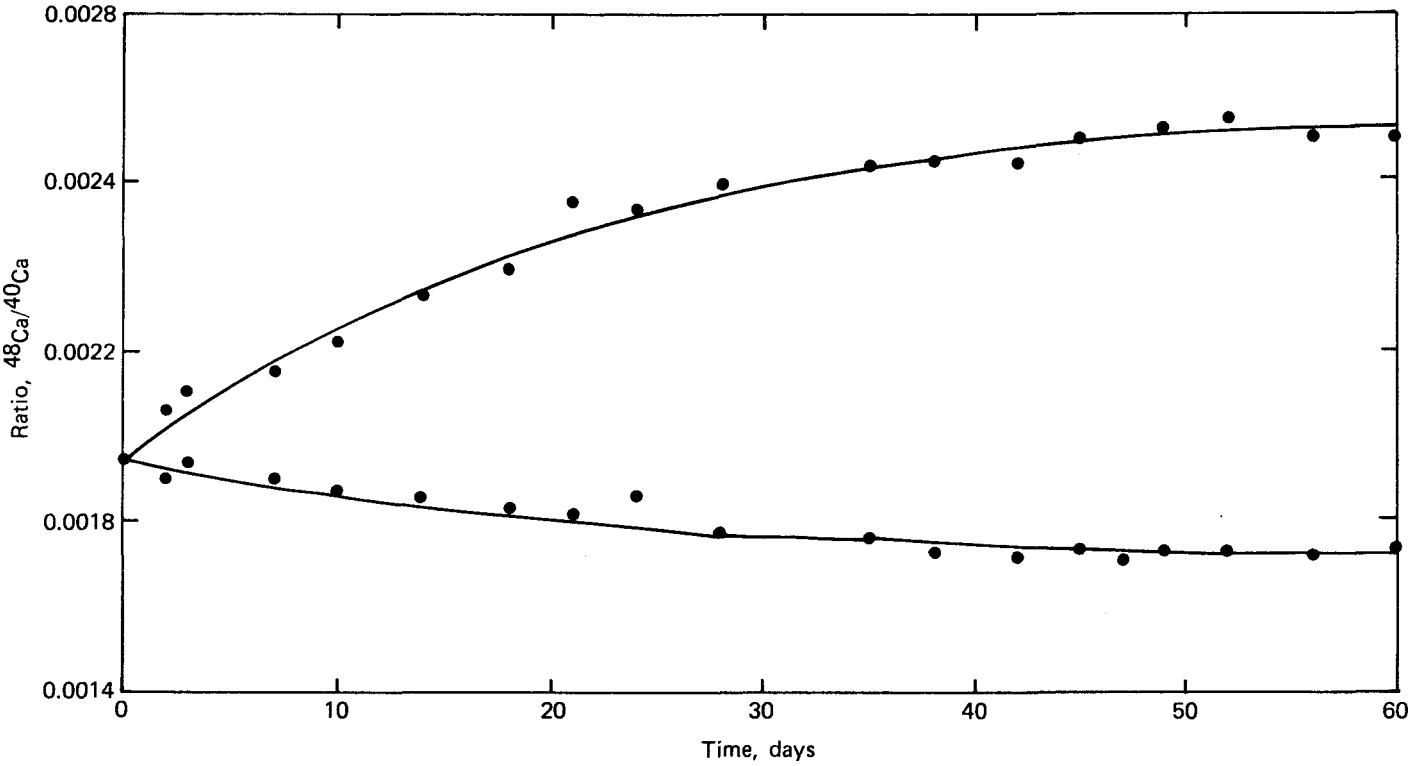

FIGURE II-5 - Calcium isotopic separation in the 114 cm liquid phase thermal diffusion column. Top solute concentration: 4.13 wt. %.

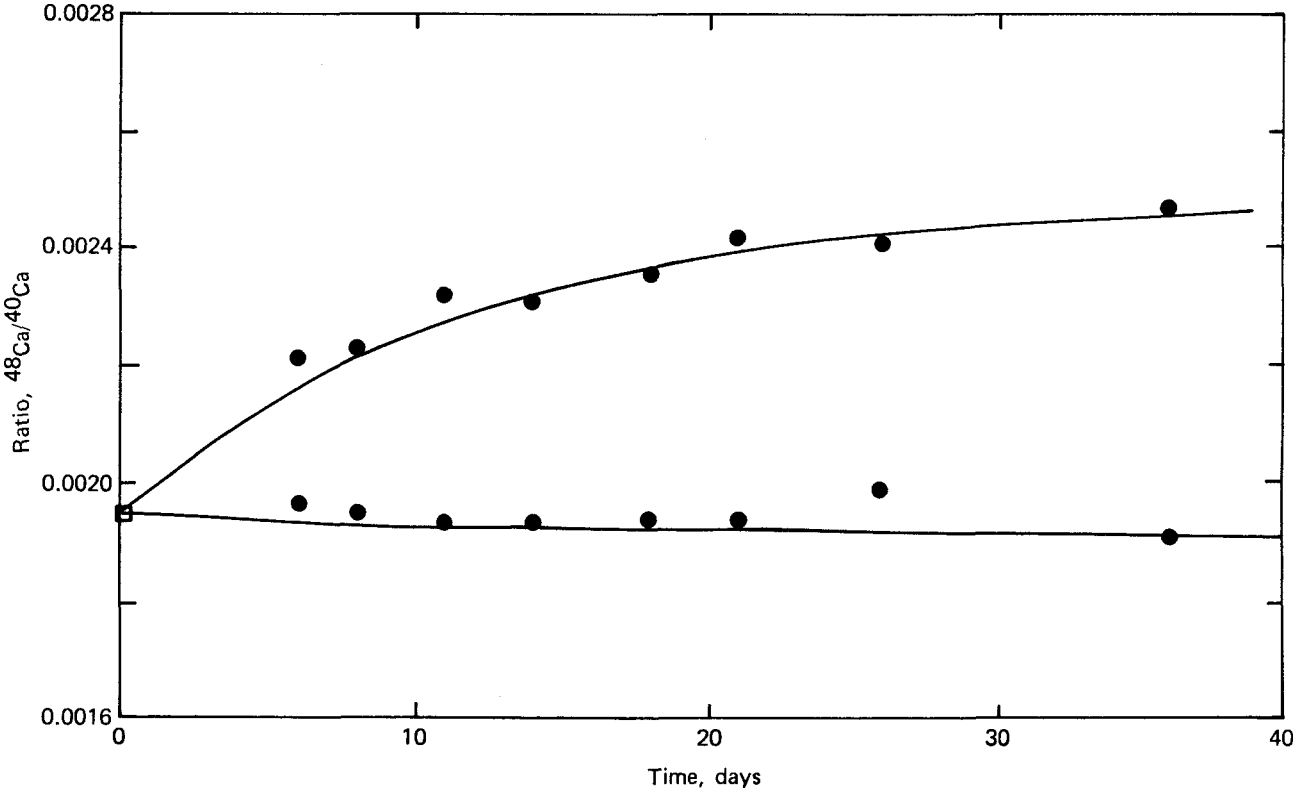

FIGURE II-6 - Calcium isotopic separation in the 114 cm liquid phase thermal diffusion column. Top solute concentration; 24.71 wt. %.

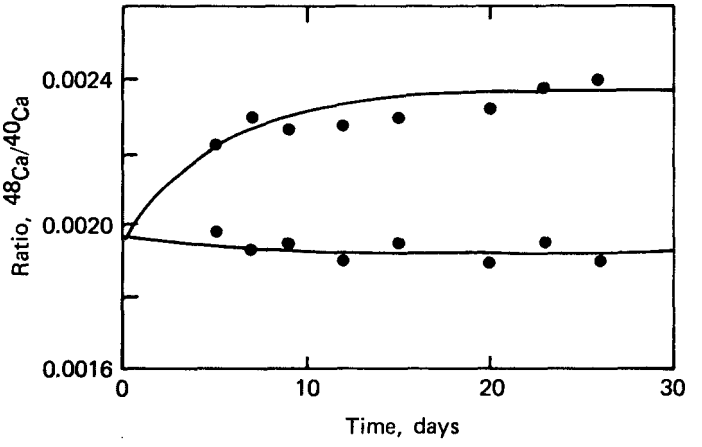

FIGURE II-7 - Calcium isotopic separation in the 15 cm liquid phase thermal diffusion column. Top concentration: 36.87 wt. %.

Table II-6 - ISOTOPIC TRANSPORT RATES FOR CALCIUM LIQUID THERMAL DIFFUSION EXPERIMENTS

Column Length (cm)	w_2(%) Top	w_2(%) Bottom	^{48}Ca Initial Transport Rate (μg/day)	Isotopic Separation Factor (q)
114	4.13	12.99	29.2	1.647
114	24.71	31.69	135	-
15	36.87	41.80	196	1.240

Mutual diffusion

W. L. Taylor and D. Cain

HE-NE AND HE-XE

In the present work we have measured mutual diffusion in equimolar mixtures of helium with neon and xenon in the temperature range from ∿350 to 1300 K. The binary diffusion coefficient, D_{12}, is defined as the positive constant of proportionality in the flux equation in units ℓ^2/t, usually given in cm^2/sec. Diffusion in gases has been comprehensively reviewed by Marrero and Mason (M&M) [13] in a lengthy treatise on the subject in 1970. Measurements for many systems were unavailable at high temperatures at that time, but M&M predicted high temperature diffusion coefficients by means of "correlation functions" based on available data with an extrapolation to high temperatures using collision cross sections obtained from molecular beam scattering. Since 1970, additional measurements [14-18] have been published with two groups conducting measurements over 1000 K [17-18]. The objectives of the present work have been to measure diffusion coefficients to temperatures in excess of 1000 K by an independent experimental method, to test the consistency of these measurements with the M&M correlations and other measured

transport properties, and to investigate various intermolecular potentials for the unlike interactions. These measurements have been made in a Hastelloy-X diffusion cell which was described in detail previously [19].

The results of the present experiments are given in Table II-7 and shown graphically in Figure II-8 by the solid circles with the M&M correlations. The other symbols represent data [14-18] not included in the M&M correlations, which are the solid lines represented by the equation:

$$\ell n(pD_{12}) = \ell nA + s\ \ell nT - \ell n[\ell n(\phi_0/kT)]^2 - S/T - S'/T^2 \quad (1)$$

with parameters given in reference 13. For He-Ne, our data rise slightly above the correlation at high temperatures as do the results of Zwackhals and Reus [18], whereas the Hogervorst data lie slightly below the line. For He-Xe, the present data cluster around the correlation over the entire temperature range. The correlations have an uncertainty of ±2% in the lower half of the range rising to ±5% in the upper half, so the majority of the data lie within these limits. It should also be noted that the very precise data of Arora, et al [16] lie exactly on the lines at 300 K. In Figure II-9 we compare the mutual consistency of our results with mixture viscosities [20] and the corresponding states principle [21]. Diffusion coefficients were derived from relationships given in the references and are calculated as percent deviations from a least squares fit to our data and the very precise 300 K result of Arora, et al [16] to

Table II-7 - BINARY DIFFUSION COEFFICIENTS OF HELIUM-NEON AND HELIUM-XENON

System[a]	Temperature (K)	D_{12}[b] (cm^2/sec)	System[a]	Temperature (K)	D_{12}[b] (cm^2/sec)
He-Ne	388	1.772	He-Xe (contined)	505	1.351
	446	2.219		506	1.302
	548	3.100		578	1.645
	586	3.434		632	1.982
	669	4.171		658	2.106
	670	4.269		731	2.477
	771	5.490		744	2.557
	866	6.627		794	2.753
	882	6.840		818	3.068
	947	8.074		883	3.469
	952	7.727		942	3.843
	1014	9.285		996	4.385
	1027	9.314		1016	4.600
	1075	10.142		1057	4.688
	1129	10.791		1080	4.974
	1199	12.360		1107	5.314
				1145	5.424
He-Xe	351	0.736		1155	5.831
	418	0.980		1179	5.780
	477	1.173		1217	5.938
	498	1.245		1252	6.524
	502	1.280			

[a]Feed gases were research grade cylinder gases of >99.9% purity.

[b]Corrected to one (1) atmoshpere pressure.

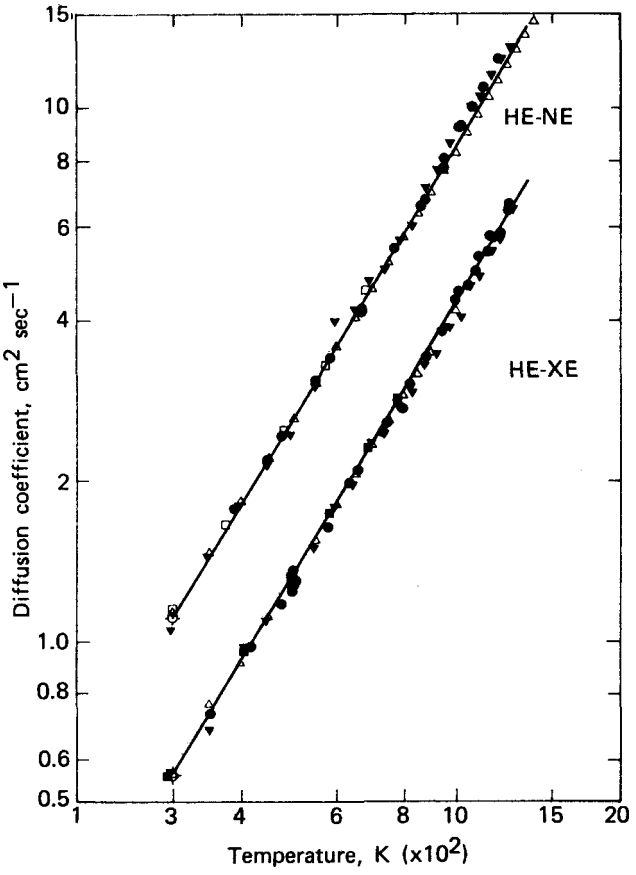

FIGURE II-8 - Equimolar diffusion coefficients at one atmosphere for He-Ne and He-Xe as a function of temperature. The solid lines are the respective M&M correlation functions [13]. The experimental points are those measured subsequent to and not included in the correlations. They are: a) He-Ne ●, present data; △, Hogervorst [17]; ▼, Zwackhals and Reus [18]; □, Kalinen and Suetin [15]; and ⊹, Arora, et al [16]. b) He-Xe, same as above except ■, Loiko, et al [14].

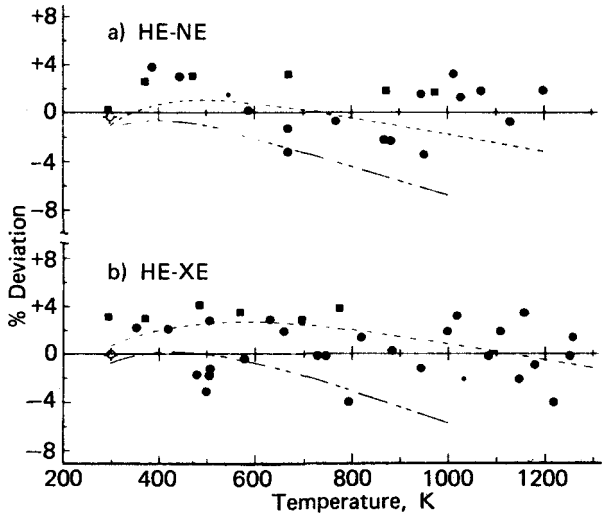

FIGURE II-9 - Mutual consistency of the present diffusion data with mixture viscosities, corresponding states, and the earlier diffusion data. The baselines represent the present data and the Arora, et al 300 K data fitted by least squares to a M&M type function with the ϕ_o term fixed. The symbols and curves are as follows: ●, present data; ⊹, Arora, et al [16]; ■, D_{12} from mixture viscosities; ---, M&M correlation [13]; and — --. D_{12} from corresponding states [21].

determine the baseline. Our data have average deviations of ±2.1% and ±1.8% for He-Ne and He-Xe, respectively. Agreement with the M&M correlations are within ∿2% and within 3 to 4% for mixture viscosities. Corresponding states predictions are good around room temperature but drop off rather badly at high temperatures. This is attributed to a weakness in the correspondence when helium is one of the mixture components. Several intermolecular potentials were used to calculate theoretical diffusion coefficients which were compared to a correlation of all the data shown in Figure II-8. The HFD potential by Ahlrichs, et al [22] predicted values within 2% for He-Ne, whereas the HFD potential by Smith, et al [23] was best for He-Xe. Theoretical values were about 2% low over much of the range, dropping to ∿5% low at the highest temperatures. We conclude that the diffusion coefficients for the He-Ne and He-Xe systems are defined within a few percent from 300 to 1300 K. Values for D_{12} are also in

reasonable agreement with other measured properties and can be predicted fairly accurately by the HFD intermolecular potential.

HE-, NE-, AND XE-AR

We have reported in detail the mutual diffusion coefficients of He-, Ne-, and Xe-Ar in Reference 24 and in earlier reports in this series. Since that time we have continued to be concerned about the abnormally large scatter in the Ne-Ar data, and the apparent inconsistency with the conclusions drawn from the other two systems. We have all along attributed the problem to the inability to discriminate the $^{20}Ne^{+}$ peak from the $^{40}Ar^{++}$ peak in the mass spectrometric analysis. We then reanalyzed our natural abundance Ne-Ar data by using the reported composition of ^{22}Ne in the mixtures. These results differed somewhat from our values reported previously [25] and exhibited an unacceptably large scatter because of the much smaller mole fraction of ^{22}Ne present in the samples. We therefore conclude that only those experiments that used ^{22}Ne as the feed gas (see Table II-6 in Reference 25) should be considered reliable. To these ^{22}Ne experiments should be added the values: D_{12} = 0.441 (0.454), 1.254 (1.291), 1.281 (1.318), and 1.990 (2.047) cm^2/sec at T = 357, 656, 661, and 861 K, respectively. The first number is D_{12} for ^{22}Ne-Ar and the second number (in parentheses) has been mass corrected to natural abundance Ne-Ar. The composite data for all three systems are shown in Figure II-10. The solid lines are the M&M correlations [13]; the other symbols represent other published results [14-18, 26-28] subsequent to and not included in the correlation. The post-1970 data shown in Figure II-10 were fitted to Equation 1, and the parameters so determined are shown in Table II-8.

Figure II-11 shows the present data (solid circles) as percent deviations from a M&M-type function whose parameters were determined by least squares and are given in the caption for Figure II-11. The ϕ_o term in the correlating function was fixed by the sources also referenced there, and all other parameters were determined from the data. The solid and half-shaded squares represent diffusion values obtained from mixture viscosities while the broken lines (— - and __ --) represent diffusion values from corresponding states and thermal diffusion, respectively. The dashed line (---) represents the original M&M correlations [13].

In Figure II-11 the average deviation of the He-Ar data is $\pm$1.5% around the baseline. This is only slightly below the original M&M correlation (<2%) and certainly well within the mutual uncertainty of the expressions. Similarly, the present results are in excellent agreement with the thermal diffusion correlation. The mixture viscosity and corresponding states results agree fairly well in the lower half of the temperature range but drop off at high temperatures. About half of the mixture viscosity points agree better with the present data than with the corresponding states calculation. It should be noted that helium may not follow the corresponding states principle as closely as the heavier noble gases do. In any event the curve is terminated at 1000 K, which is the upper limit of the universal empirical function, Ω_{11}.

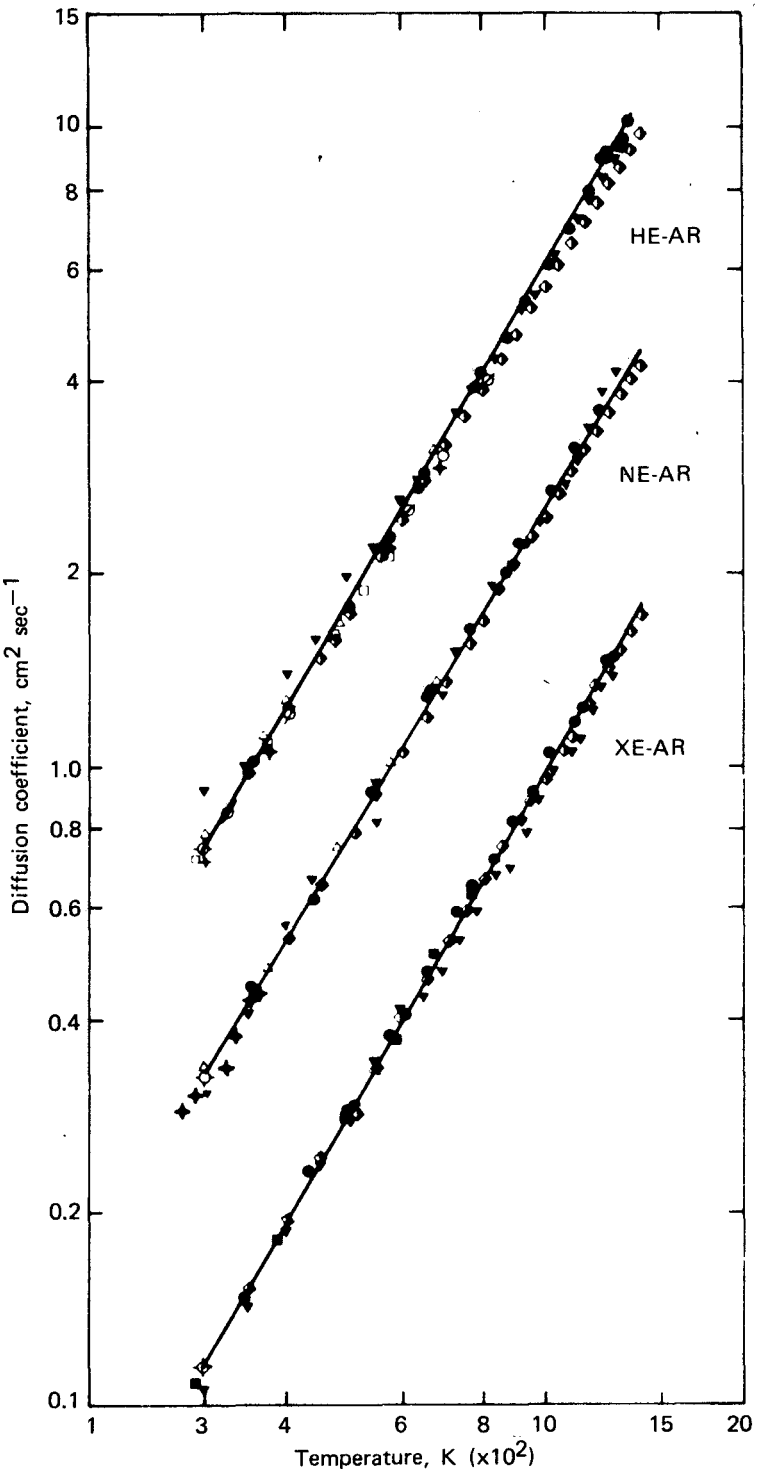

FIGURE II-10 - Equimolar experimental diffusion coefficients at one atmosphere pressure for He-, Ne-, and Xe-Ar as a function of temperature. The solid lines are the respective Marrero and Mason correlation functions [13]. The experimental points are those measured subsequently to and not included in the correlations. They are: (a) He-Ar ●, present data; ◇, Hogervorst [17]; , Zwakhals and Reus [18]; △, Kalinen and Suetin [15]; □, Seutin et al, glass capillary, and +, metal capillary [26]; Ø, Liner and Weissman [27]; and Arora, et al [16]. (b) Ne-Ar same as above except +, Nain and Saxena [28]. (c) Xe-Ar same as above except ■, Loiko, et al [14].

Table II-8 - CORRELATION FUNCTION PARAMETERS (Eq. 1) FOR DIFFUSION DATA SUBSEQUENT TO 1970

System	10^3 A	s	10^{-8} ϕ_o/k	S	S
He-Ar	15.70	1.530	9.2931[a]	-9.991	0
Ne-Ar	9.922	1.498	0.7074[a]	-36.71	1.427×10^4
Xe-Ar	9.459	1.473	36.8[b]	-101.8	0

[a]Value of ϕ_o taken from Self Consistent Field-Hartree Fock (SCF-HF) calculations in Ahlrichs, et al [22].

[b]Value of ϕ_o obtained from molecular beam scattering data with details given in Marrero and Mason [13].

In Figure II-11b the Ne-Ar data are compared to other transport data. The average deviation of the data around the baseline is once again ±1.5%. The diffusion coefficients calculated from mixture viscosity, corresponding states, and thermal diffusion agree with the present data and the M&M correlation at the lower temperatures, but fall to a maximum of from 4 to 6% below at higher temperatures.

The experimental results for Xe-Ar are shown in the lower part of Figure II-10 and in II-11c. In this case the present data and those of most other workers cluster around the M&M correlation. The exception is the results of Zwakhals and Reus whose data lie for the most part significantly below the rest. In Figure II-11c our measurements scatter around the baseline with an average deviation of ±1.8%. Diffusion coefficients calculated from mixture viscosity, corresponding states, and thermal diffusion all appear to be mutually consistent with the directly measured values. It is interesting, however, that the mixture viscosity results fall on the opposite side of the baseline from those derived from corresponding states.

Molecular beam scattering

TRIPLE PUMPED DETECTOR

R. W. York

The molecular beam triple pumped detector system [36] was installed on the beam chamber for initial vacuum testing. It was found that the modified mounting seal had an excessive leak resulting from a design adaptation to the original configuration. This necessitated the removal of the detector housing from the chamber and the remachining of the mounting flange to accept a new vacuum seal design. This new seal was installed and another vacuum test of the system had been performed. The latest test successfully showed a leak-tight system while rotating the detector under vacuum conditions.

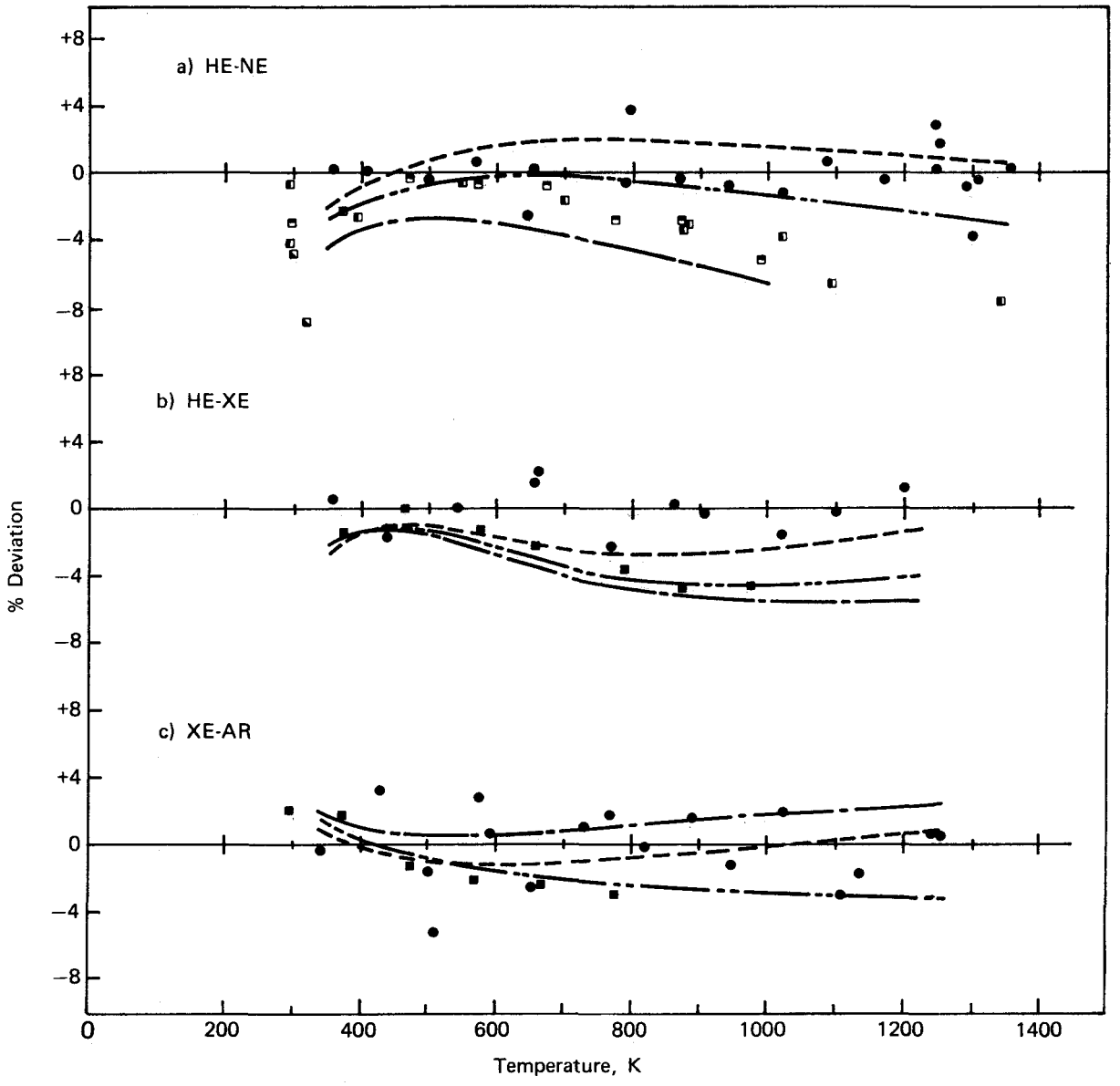

FIGURE II-11 - Mutual consistency of the present diffusion data with mixture viscosities, corresponding states, and thermal diffusion data. The baselines represent the present data fitted by the method of least squares to the M&M-type function given by Eq. 1 with the ϕ_o term fixed. The symbols and curves are as follows: (a) He-Ar baseline parameters, ϕ_o/k = 2.931 x 10^7 [10], A = 7.060 x 10^{-3}, s - 1.640, S = -71.17, and S' = 0; ●, present data; half-shaded squares, D_{12} calculated from mixture viscosities; ◓; [29a]; ◧, [29b]; ◹ , [29c]; ---, M&M correlation [13]; ——, D_{12} calculated from corresponding states theory [30-32]; and — --, D_{12} calculated from thermal diffusion factor correlations [33]. (b) Ne-Ar baseline parameters, ϕ_o/k = 7.074 x 10^7 [10], A = 0.4523, s = 1.034, S - 6.534 x 10^2, and S' = -9.586 x 10^4; ■, D_{12} calculated from mixture viscosities [34]; the curves are the same as above. (c) Xe-Ar baseline parameters, ϕ_o/k = 3.68 x 10^9 [13], A = 1.113 x 10^{-2}, s = 1.456, S = 1.248 x 10^4, and S' = 0; ■, D_{12} calculated from mixture viscosities [35]; the curves are the same as above.

Evacuation of the chamber produced an unexpected vertical deflection of the detector housing of 0.049-in. This made it necessary to realign all of the beam-forming components to compensate for this detector movement. These precision alignment procedures were described previously [37].

The ionizer was installed in the upper portion of the innermost triple pumped region with its associated internal wiring routed independently through the vacuum wall in the top rotary section. The quadrupole/electron multiplier assembly was fitted to the lower portion of the detector housing, placing it in the doubly pumped vacuum region. The associated RF and high voltage wiring was routed through the housing vacuum wall to a rotation loop configuration which was connected to the external electronics via a feedthrough in the beam chamber vacuum wall. Final installation of the support electronics and complete operational testing will be completed before the system is used for experimental measurements.

VELOCITY SELECTOR

P. T. Pickett

The differentially pumped detector assembly on the bell jar test system containing the velocity selector was fitted with a LN_2 cold trap and isolation gate valve above the intermediate diffusion pump to provide a lower ultimate pressure and to prevent detector contamination from diffusion pump oil backstreaming. Initial pumpdown tests showed that the cold trap reduced pumping speed without providing any significant pressure improvement. It was therefore removed, as was the LN_2 cold trap on the main bell jar section, in order to allow the diffusion pumps to produce the maximum pumping speed possible. Actual velocity selector experiments will begin as soon as this final configuration pumps down to a stable pressure.

TOTAL CROSS SECTIONS

W. L. Taylor

In the previous report [38] in this series, we calculated theoretical total cross sections for the He-Ar system using a semi-classical approach. We used the WKB (Wentzel-Kramers-Brillouin) approximation to evaluate the scattering phase shifts, η_ℓ, which were summed to evaluate the total cross section. These calculations were carried out for the velocity range 800 to 2000 m/sec using seven He-Ar interatomic potentials which are listed in Table II-7 in Reference 38. A comparison was made with the experimental data in Table II-9 of Reference 39, which were fitted to a suitable function by the method of least squares. The resulting figure (Figure II-13, Reference 38) displayed the comparisons as percent deviations of the theoretical calculations from the Mound data. We noted at that time that our data may be a few percent high; thus we have chosen to test the potentials against a composite of all available (deconvoluted) experimental cross sections for He-Ar. Deconvoluted cross sections [40-43] are shown in Figure II-12. Most of the Beier data deviated by more than 3σ from the remainder and our fitting function did not allow for the peak in the low temperature data of Grace, et al. These points were thus excluded.

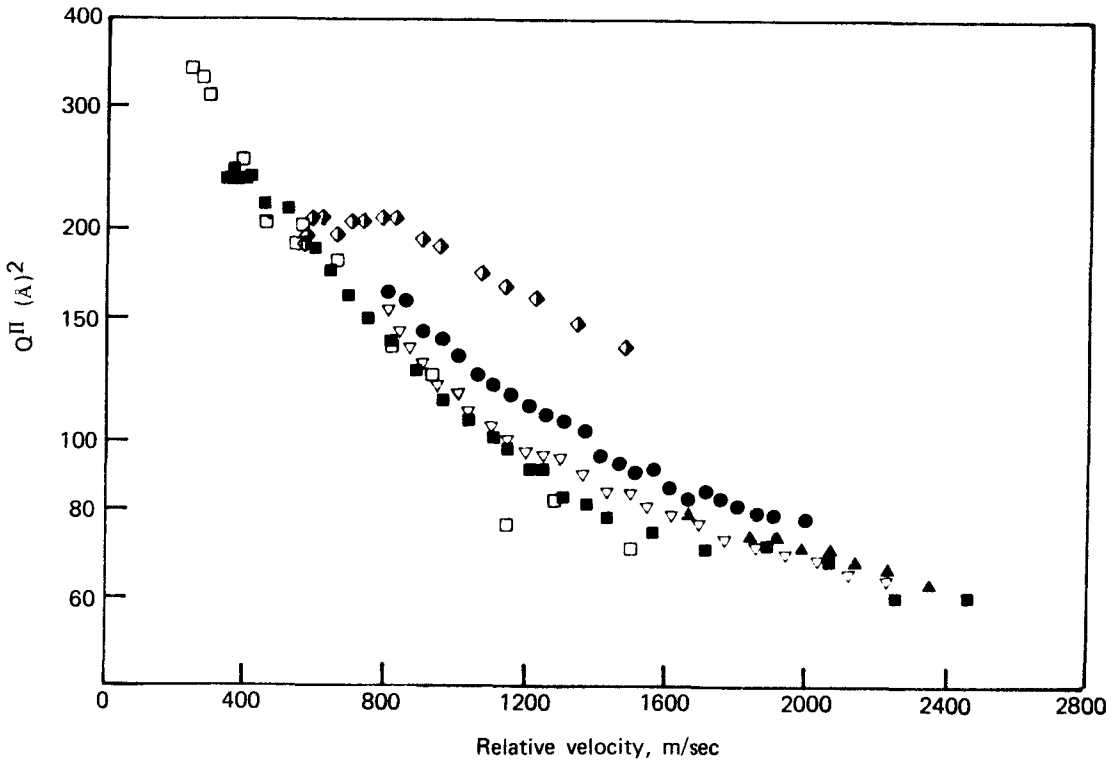

FIGURE II-12 - The deconvoluted cross section, Q^{II}, as a function of the average relative velocity, $\bar{v}_r$, for He-Ar. The experimental points are: ●, present data, He (beam) - Ar (target) [39]; ■, Helbing, et al [40]; ▲, Eckelt, et al [41]; ◆, Beier [42]; ▽, Pirani and Vecchiocattivi [43]; and □, Grace, et al [44].

The remaining data fit the equation:

$$Q^{II}(v_r) = A + B/v_r + C/v_r^2 \qquad (1)$$

with an average deviation of 7.9% with the parameters A = 13.156; B = 1.1697 x 10^5; C = -9.997 x 10^6. A comparison of the total cross sections calculated with the seven potentials and compared to the composite data is shown as a percent deviation plot in Figure II-13. Percent deviations as represented by % Dev = $(Q_{Th} - Q^{II})/Q^{II}$ x 100, with Q^{II} obtained from Equation 1 and Q_{Th} calculated using each interatomic potential, were then evaluated for the seven cases as a function of the relative velocity. The horizontal short dashed lines represent the average percent deviation of the data. It can be seen that the region enclosed therein acts as a coarse filter for the potentials. The HFD provides the best representation, with the MS, M-6-8, and M^2SV potentials well within the uncertainty. DA predictions for the cross sections are generally too high, and the ESMSV predictions are mostly low. Large deviations arise for all potentials at low relative energies. This may either be due to the very low temperature data of Grace, et al [44] or to a breakdown of the semi-classical calculation at low relative velocities. Further investigations will focus on this subject.

Potassium isotope enrichment

B. E. Jepson and G. C. Shockey

Potassium isotope enrichment by chemical exchange with 222 cryptand was investigated. The resin-bound cryptand used in this work has been described in more detail in previous reports of this series.

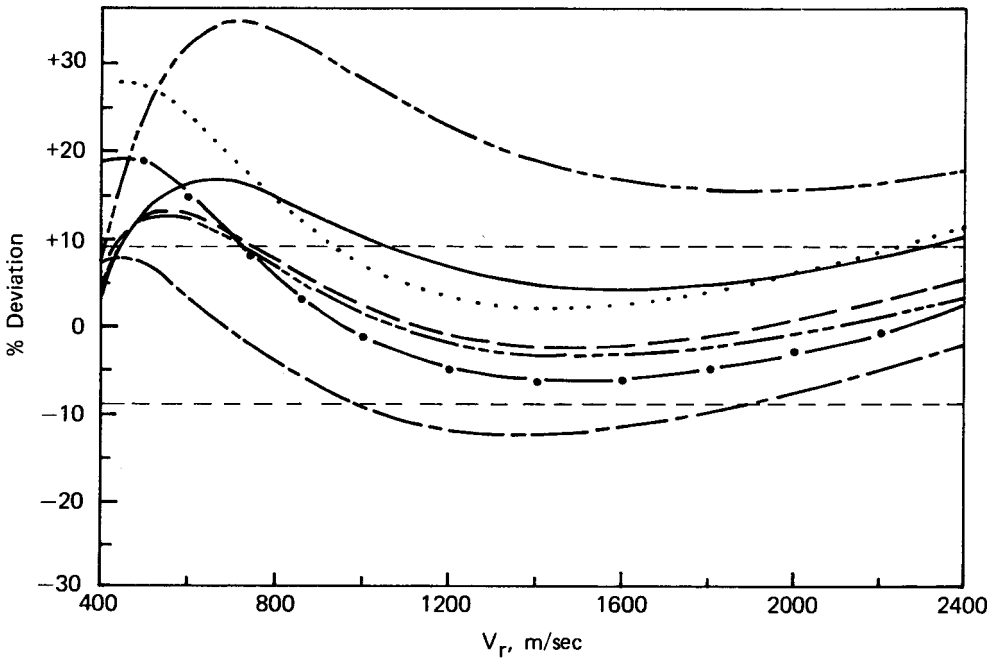

FIGURE II-13 - Percent deviation of He-Ar interatomic potentials from the composite experimental data represented by Eq. 1. The theoretical curves are: ——, DA [45,46]; —— --, Exp-6 [47]; —— -, ESMSV [48]; ---, HFD [49]; ····, M-6-8 [50]; —— ---, MS [51]; and —— •, M^2SV [52]. Horizontal dashed lines represent average percent deviation of composite data.

An adsorption isotherm developed for aqueous KCl solutions and the resin is shown in Figure II-14. The resin capacity for potassium complexation from aqueous solution was approximately 0.16 meq/gm dry resin. A jacketed chromotographic column 58 cm long and 0.9 cm in diameter was used for the isotopic enrichment study. A 0.01N KCl solution passed through the column using the breakthrough elution technique yielded the potassium concentration profile shown in Figure II-15. All potassium concentrations were measured with an ion specific electrode.

The number of theoretical stages, N, can be estimated from the breakthrough elution curve in Figure II-15 by the method derived by E. Glueckauf [53]. The derivation yields the expression $N = 2\Pi(\bar{V}/\Delta V)^2$ where $\bar{V}$ represents total volume eluted to reach the inflection point of the curve (see Figure II-15) and ΔV the net volume eluted in the breakthrough region alone. The number of stages calculated from this expression is 340. The derivation, however, is based on the assumption of a linear adsorption isotherm; and as can be seen in Figure II-14, the isotherm departs from linearity in the region of 0.01 N KCl in the aqueous phase. As a consequence of this non-linearity, the estimate of theoretical stages may be inaccurate. After the column was fully loaded, the potassium was eluted with water.

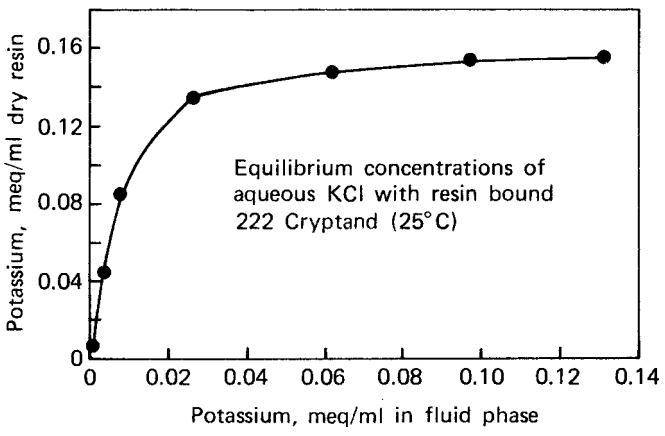

FIGURE II-14 - Potassium adsorption isotherm.

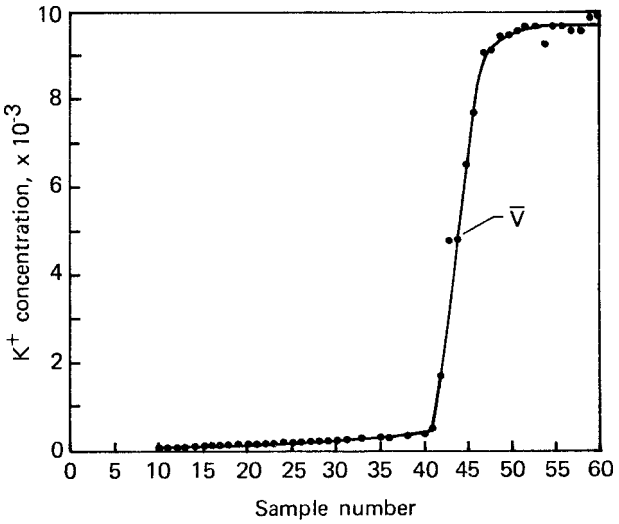

FIGURE II-15 - Breakthrough elution curve of aqueous KCl and 222 cryptand resin.

Samples were converted from KCl to KNO_3 and analyzed for isotopic composition by mass spectrometry. The results are shown in Table II-9. Although the rear elution curve appeared to show a very slight enrichment of potassium-41 relative to the breakthrough curve, the difference is on the order of the uncertainty of the analyses, and no definite conclusions can be drawn regarding the precise size and direction of the isotope effect. It can be concluded, however, that the isotope effect is too small to be of practical value.

Table II-9 - POTASSIUM 41 CONCENTRATIONS IN ATOM %

Breakthrough Curve		Rear Elution Curve	
Sample	K-41, %	Sample	K-41, %
27	6.70	117	6.73
32	6.69	120	6.82
37	6.68	122	6.76
42	6.70	124	6.69
47	6.68	126	6.73
52	6.70	128	6.73
57	6.67		
62	6.74		

III. Metal hydride studies

New lanthanide hydride compounds

G. L. Silver and A. B. Nease

In 1980, Silver reviewed the results of research on a curious new class of hydridic rare earth compounds [1]. These compounds are prepared by the dissolution of rare earth metals in selected acids such as acetic acid. This dissolution reaction is the only method for preparing the compounds which appear to be oxide-hydride compositions [1]. The purpose of this section is to describe what appears to be another method for preparing these compositions, but this new method is inferior to metal dissolution as a route to the compounds. The new method apparently produces the compounds as impurities on substrates of rare earth hydroxides.

It has been known for many years that the lanthanide metals absorb hydrogen with the formation of the hydride. The hydride-forming reaction may be summarized as follows:

$$Ln + 3/2\ H_2 = LnH_3 \qquad (1)$$

It has also been known for many years that the lanthanide hydrides are decomposed by water producing the lanthanide hydroxides.

$$LnH_3 + 3HOH = Ln(OH)_3 + 3H_2 \qquad (2)$$

But careful observation of the hydrolysis reaction reveals that the reaction product may have a color not characteristic of the parent lanthanide hydroxide. Cerium, neodymium, and samarium hydrides were prepared by washing chips of the metals with acetone and drying in a vacuum. The metal chips were then heated to 500°C in vacuum. Hydrogen at a pressure of about one atmosphere was kept above the chips as they cooled to room temperature and was then removed from the glass vessel containing the granular hydride. The vessel was opened in an atmosphere of argon, and water was poured onto the hydride so that the hydride was immersed to a depth of about one centimeter. Gas bubbles were released as the hydride slowly began to hydrolyze; once the hydrolysis reaction began, the rate of hydrolysis accelerated. The product of the hydrolysis was a voluminous precipitate which ought to have been white in the case of cerium [$Ce(OH)_3$], pale blue in the case of neodymium [$Nd(OH)_3$], and white in the case of samarium [$Sm(OH)_3$]. In fact, a black precipitate was produced by the hydrolysis of the cerium hydride, a brown precipitate by the hydrolysis of the neodymium hydride, and a yellow precipitate by the hydrolysis of the samarium hydride.

The colors of new lanthanide hydride compounds are black in the case of cerium, brown in the case of neodymium, and yellow in the case of samarium [1]. Moreover, the black, cerium-based compound is quite unstable and soon decomposes. The black precipitate produced by the hydrolysis of the cerium hydride also showed instability, as it soon turned from black to white, indicating decomposition of whatever material was responsible for the initial black color. The brown and yellow colors of the products of the hydrolysis of NdH_3 and SmH_3 were much more stable, however. These observations on the colors

of the products of the hydrolysis of lanthanide hydrides suggest that Equation 2 is incomplete and should be expanded as follows (neglecting stoichiometry coefficients):

$$LnH_3 + HOH = Ln(OH)_3 + H_2 + \text{(a species of the new oxide-hydride compounds [1])}. \quad (3)$$

If the essence of Equation 3 is correct, it apparently means that uninegative hydroxide ions (OH^-) substitute for uninegative acetate ions (and probably hydride ions as well) when the new hydride compounds are formed by the hydrolysis of hydrides.

Several attempts to prove the existence of the new compounds dispersed on the rare earth hydrides were made, but none of them were definitive - perhaps because the yield of the new compounds in the hydrolysis reactions is so small. The following observations were made, however:

1. When heated to 1000°C in vacuum the dried Nd based hydrolysis product released 20.95 ml of gas per gram of sample, whereas the samarium hydrolysis product released only 3.21 ml per gram of sample. The new compounds are known to release hydrogen when heated [1], but hydrogen release in the present case may be due to some residual lanthanide hydride not hydrolyzed by the water (see Equation 3).

2. The x-ray powder diffraction patterns of the products of lanthanide hydride hydrolysis showed only lines that were characteristic of the corresponding metal hydroxides. The failure to observe lines due to the new compounds may only indicate a low percentage of these new compounds on the hydroxide substrates, however.

3. Analysis of the preparations indicated 86.2% Nd and 1.62% H, and 79.3% Sm and 1.58% H in the neodymium and samarium preparations, respectively. The principal metallic impurities in the preparations were other rare earth elements, and all other impurities were at levels less than 100 ppm each.

4. Thermogravimetric analysis of the hydroxide preparations showed two regions of weight loss for both preparations. In the case of the neodymium preparation, the first region of weight loss was between 252°C and 319°C, and amounted to 10.3% of the sample weight. The second region of weight loss was between 426°C and 440°C, and amounted to 3.6% of the sample weight. For the samarium preparation, the first region of weight loss was 248°C to 292°C, and amounted to 11.2% of the sample; the second region was 393°C to 410°C, and amounted to 2.8% of the sample weight. Thermogravimetric analysis of the new compounds has also indicated weight loss upon heating [1].

5. The photoacoustic spectrum of the neodymium hydrolysis preparation was similar (in location of peaks) to the photoacoustic spectrum of Nd_2O_3. Peak intensities were much greater in the neodymium oxide, however. (The region scanned was 200-900 nm.) The photoacoustic spectrum of the samarium compound showed activity between 1000 and 1500 nm.

6. Differential thermal analysis of the compounds showed an endotherm at 345°C for the neodymium preparation, but a curious leak of thermal activity for the samarium preparation between room temperature and 500°C.

7. When maintained in evacuated glass tubes, both compounds showed gradual color change in portions of the samples exposed to light. The neodymium hydrolysis preparation gradually lost its brown color and turned bluish-grey, whereas the samarium compound slowly turned white.

8. The infrared spectra of the compounds were obtained in a Nujol mull and in a KBr pellet. There was little difference between the spectra of the hydrolysis preparations and the spectrum of Nd_2O_3 when obtained in mineral oil. In the KBr pellet, two bands were observed near 1400 cm^{-1}. This may represent carbonate impurity. Another band was observed near 675 cm^{-1}, and a strong, sharp band at 3600 cm^{-1} which may represent the OH stretching vibration of a metal hydroxide. The Raman spectra of the hydrolysis preparations were also examined. Raman scattering was quite weak: only weak bands at 475 cm^{-1} and 2240 cm^{-1} were observed. The band at 2240 cm^{-1} could be the result of a metal-hydride vibration.

Acknowledgement

The authors wish to thank D. B. Sullenger for the powder diffraction patterns.

Hydrogen diffusion in crystalline and amorphous titanium-copper hydrides

R. C. Bowman, Jr.

The properties of amorphous alloys (i.e., the metallic glasses) and the behavior of hydrogen in metals are two of the most active research areas for the transition metals. Diffusion behavior of the hydrogen isotopes has also been extensively evaluated [2-5] in crystalline metals and alloys. However, the specific roles of crystal structure on the diffusion mechanisms in glassy metals and metal-hydrogen systems remain poorly understood and controversial.

Although there is a vast literature on the properties of crystalline metal-hydrogen systems that dates back over several decades, the first report of an amorphous metal-hydrogen system (i.e., a-$Ti_{1-y}Cu_yH_x$) was published by Maeland [6] in 1978. There have been several subsequent papers on amorphous a-$Ti_{1-y}Cu_yH_x$ [7-9] as well as other glassy metal-hydrogen systems [10-15]. Furthermore, low concentrations (i.e., 1 atm %) of hydrogen exert a major influence on the mechanical relaxation properties in many diverse metallic glasses [16-19]. Since amorphous alloys and metal hydrides have many potential technological applications as well as inherently interesting fundamental properties, research on the amorphous metal-hydrogen systems has grown rapidly with the expectation for improved understanding of both material classes.

The present study addresses the roles of crystal structure on the interstitial site occupancy by hydrogen atoms and hydrogen diffusion behavior in crystalline $TiCuH_x$ and Ti_2CuH_x and the amorphous hydride a-$TiCuH_{1.4}$. This task has been accomplished by nuclear magnetic resonance (NMR) measurements of the proton lineshapes and relaxation times, which are extensions of previous studies [9,20].

The $Ti_{1-y}Cu_yH_x$ system is a favorable candidate for comparative studies of crystalline and amorphous metal hydride phases. Metallic glasses form readily in the $Ti_{1-y}Cu_y$ system over the wide composition range of 30-70 atm % Cu which includes the crystalline intermetallic compounds TiCu and Ti_2Cu. Both TiCu and Ti_2Cu have been found [6,8,21] to form ternary hydrides with limiting compositions $TiCuH_{1.0}$ and $Ti_2CuH_{2.80}$. Under suitable conditions the corresponding $Ti_{1-y}Cu_y$ glasses can also absorb hydrogen without crystallization [6,8] to form amorphous hydrides such as a-$TiCuH_x$ where $1.2 \leq x \leq 1.4$. The present experiments confirm the previous assertion [9,20] that crystal structure has a dominant role in the diffusion behavior for both crystalline and amorphous $Ti_{1-y}Cu_yH_x$ phases. The occupancy of more diverse interstitial sites (i.e., Ti_4Cu_2 sites, for example, in addition, to the preferred Ti_4 sites) in Ti_2CuH_x and a-$TiCuH_{1.3\pm0.1}$ greatly enhances the observed hydrogen mobility (with an accompanying decrease in activation energy E_a) in these phases relative to the diffusion rates in $TiCuH_{0.94}$ and γ-phase TiH_x.

The intermetallic TiCu crystallizes with a tetragonal structure of the B11 type. This structure is illustrated in the upper portion of Figure III-1 where the interstitial sites occupied by the H-atoms are also shown. When TiCu is exposed to hydrogen gas and the temperature is maintained below 200°C, a ternary hydride $TiCuH_{1.0}$ forms [6] with a 9% volume increase but no change in the metal host structure. In a neutron diffraction study of $TiCuD_{0.90}$, Santoro et al [22] determined the crystal structure in Figure III-1 where the D-atoms only occupy the interstitial sites with four Ti nearest neighbors. The tetrahedral site occupancy of H-atoms in crystalline $TiCuH_{0.93}$ has also been verified by inelastic neutron scattering measurements [7], whereas the second moment (M_{2D}) for the proton lineshape [20] in $TiCuH_{0.94}$ agrees with the structure in Figure III-1. The absence of H-atoms from the other interstitial sites, which always include several Cu atoms as nearest neighbors, is not surprising since copper is an endothermic absorber of hydrogen with no known stable hydride phases. When the crystal structure of the fcc γ-phase TiD_2 structure (Figure III-1a) is compared with the TiCuD structure (Figure III-1b), it is clear that the double layer of Ti atoms in TiCuD gives a two-dimensional analog of the TiD_2 structure. Because a double layer of Cu atoms separates each 2-D TiH_x layer, diffusion in crystalline $TiCuH_x$ is restricted to jumps between nearest-neighbor tetrahedral sites within the H-atom plane, whereas jumps through vacant octahedral sites are possible [23,24] in fcc γ-TiH_x. In fact, the relatively large E_a value for the proton relaxation times in crystalline $TiCuH_{0.94}$ has been attributed [5,20] to higher activation energies for the direct jumps between the neighboring sites compared to the lower energy required [23] to jump through the vacant octahedral sites in γ-TiH_x.

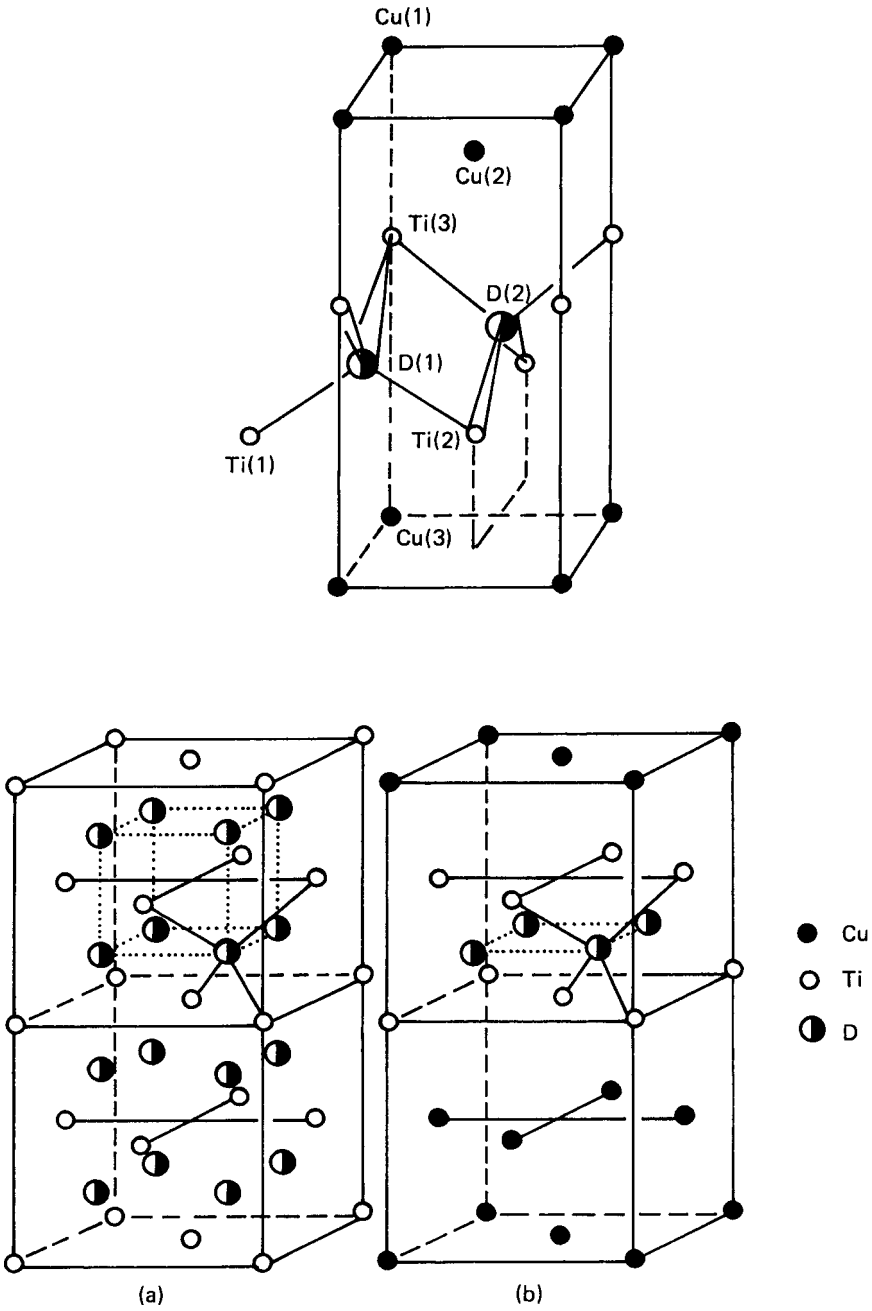

FIGURE III-1 - Comparison of structures of (a) TiD_2 and (b) TiCuD where for clarity the unit cell (upper figure) is doubled.

If ternary TiCuH is heated above 250°C for extended times [6,20], it will disproportionate into a mixture of γ-TiH_x and Cu metal. Similarly, when TiCu alloy is heated above 250°C and exposed to hydrogen gas, it will form [25] the segregated TiH_x + Cu mixture and not the ternary phase $TiCuH_{1.0}$. Maeland [6] has shown by a thermodynamic analysis of the free energies that the ternary $TiCuH_{1.0}$ phase is unstable with respect to TiH_2 + Cu. The formation of metastable $TiCuH_x$ below 200°C occurs because the metal atom mobilities are too slow to permit attainment of the equilibrium products TiH_2 and Cu metal.

The crystal structure of Ti_2Cu is tetragonal of the type $C11_b$ and is illustrated in Figure III-2. The Ti_2Cu structure is very similar to the TiCu structure except the double layers of Ti atoms in Ti_2Cu are separated by a single Cu layer instead of the double layer as in the TiCu structure. The presumably preferred Ti_4 interstitial site for hydrogen occupancy is also indicated in Figure III-2. At temperatures below 200°C, crystalline Ti_2Cu will absorb hydrogen to form [6,21] a metastable ternary hydride phase Ti_2CuH_x with $x \lesssim 2.8$. However, x-ray and neutron diffraction measurements [6,21,26] indicate a structure change occurs for the Ti_2CuH_x phase. A tentative analysis [26] of the neutron pattern for $Ti_2CuD_{2.5}$ suggests an orthorhombic structure with lattice parameters: a = 0.306 nm, b = 0.333 nm, and c = 1.01 nm. Since hydrogen occupancy of all the Ti_4 sites in the Ti_2Cu structure limits the composition to x = 2.0, other sites must also be occupied to yield $Ti_2CuH_{2.7\pm0.1}$. Inelastic neutron scattering [27] indicates some H-atoms do occupy octahedral

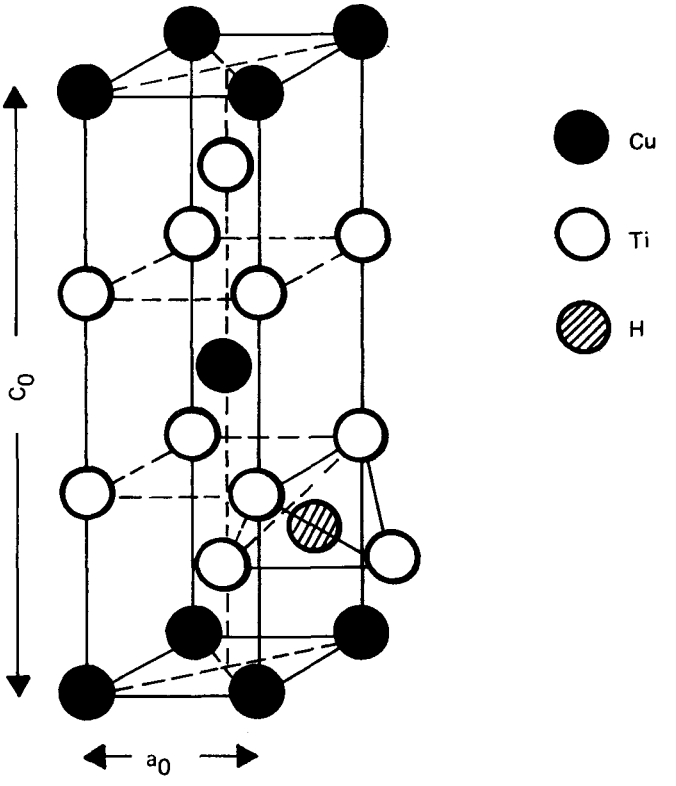

FIGURE III-2 - Crystal structure of Ti_2Cu where one of Ti_4 interstitial sites that is a preferred site for hydrogen occupancy has been identified.

sites in Ti_2CuH_x. From Figure III-2, the most likely candidates are the Ti_2Cu_4 and Ti_4Cu_2 sites in the Cu-only layers. The poor quality of the x-ray patterns [6,21] and apparent complexity of the Ti_2CuH_x structure have precluded a reliable structure determination at this time. The ternary Ti_2CuH_x phase is unstable [6,21,25] above about 200°C relative to the TiH_x + Cu mixture as previously described for the TiCu-H_2 system.

The a-$Ti_{1-y}Cu_y$ amorphous alloys are conveniently prepared by standard melt-spinning techniques. The crystallization temperatures of hydrogen-free a-$Ti_{1-y}Cu_y$

metallic glasses are found [6,8,28] to be above 300°C. Although the x-ray patterns of the a-$Ti_{1-y}Cu_y$ metallic glasses gave the broad maxima that are consistent with the absence of crystalline order, recent neutron diffraction [28,29] and EXAFS [30] experiments on amorphous a-$Ti_{1-y}Cu_y$ samples have indicated extensive chemical short range ordering in these glassy metals. These results imply that the local structures for those amorphous a-$Ti_{1-y}Cu_y$ alloys with compositions near the intermetallic phases (i.e., TiCu or Ti_2Cu) should be very similar to the structure in the corresponding crystalline phases. However, there can be a wider distribution [28-30] of local structures in the metallic glass.

The metallic glasses a-$Ti_{1-y}Cu_y$ where $0.35 \leqslant y \leqslant 0.65$ will absorb hydrogen at room temperature to form ternary amorphous a-$Ti_{1-y}Cu_yH_x$ without crystallization [6,8]. An interesting aspect of the Ti-Cu system is that the amorphous alloys absorb significantly more hydrogen than the corresponding crystalline intermetallics. This behavior has not been observed in other amorphous-crystalline alloys [10-12,14,15] and may reflect the ability of hydrogen to occupy a wider variety of Ti-Cu interstitial sites than are available in the ordered crystalline structures. A comparison of the neutron vibrational spectra [7] for crystalline $TiCuH_{0.93}$ and amorphous a-$TiCuH_{1.3}$ implies that H-atoms in the amorphous hydride occupy a much broader distribution of local environments (possibly, including some octahedral sites) with nominal tetrahedral symmetry than the single Ti_4 site occupied in $TiCuH_{0.93}$. The proton spin-spin (T_2) and dipolar (T_{1D}) relation times have indicated [9] that hydrogen mobility in a-$TiCuH_{1.3}$ is significantly greater than in crystalline $TiCuH_{0.94}$ or γ-TiH_x. Although the proton relaxations for both $TiCuH_{0.94}$ and γ-TiH_x can be represented by single activation energies over wide temperature ranges [9,20,23,31], four E_a values are required [9] to represent hydrogen diffusion in a-$TiCuH_{1.3}$ between 115 K and 420 K. The enhanced hydrogen mobility in the amorphous a-$TiCuH_{1.3}$ phase has been attributed [9] to the removal of the structural constraints [20] on the H-atom jump paths in crystalline $TiCuH_{0.94}$. However, a more complete description of the diffusion processes in the amorphous phase was not possible since detailed models of site occupancies and alternative jump paths were not available. The greater mobility in the amorphous phase is consistent with the lower thermal stability of a-$TiCuH_{1.3}$, which segregates [8,9] into the TiH_x + Cu mixture at about 425 K whereas crystalline $TiCuH_{0.94}$ does not decompose until temperature exceeds 550 K under similar experimental conditions [20].

Most of the experimental procedures employed to prepare the crystalline and amorphous samples for the present studies have been described in detail elsewhere [6-9,21] and will not be repeated. The crystalline $TiCuH_{0.94}$, $Ti_2CuH_{1.9}$, and $Ti_2CuH_{2.63}$ samples were prepared by reaction with hydrogen gas at a temperature of about 150°C. The amorphous a-$TiCuH_{1.4}$ sample was prepared at room temperature to avoid crystallization. Compositions were verified by volumetric analyses during thermal desorption at 1000°C. All the samples were handled and stored in inert atmosphere gloveboxes prior to loading the NMR tubes, which were subsequently evacuated and flame-sealed.

The proton lineshapes were measured with a simplified version [32] of the magic-echo sequence and the second moments (M_{2D}) were determined from Gaussian plots of the initial portions of the lineshape decays. The magic echoes were measured at a proton resonance frequency of 56.4 MHz on a wide-band transient spectrometer that was previously described [32]. A different spectrometer [20] was used to measure the rotating frame relaxation time ($T_{1\rho}$) at a proton resonance frequency of 34.5 MHz and spin-locking magnetic field of nominally 7.3 G. The total temperature range of the NMR experiments was 80 K to 550 K; however, the amorphous a-$TiCuH_{1.4}$ was not heated above 420 K to prevent the decomposition previously observed [9].

The crystalline $TiCuH_{0.94}$ and Ti_2CuH_x samples yield room temperature proton spectra with the nearly Gaussian lineshapes that are expected [2] for immobile "rigid-lattice" nuclei. However, a motionally narrowed exponential decay is observed [9] at room temperature for the proton spectra in the amorphous a-$TiCuH_x$ samples. When the a-$TiCuH_x$ samples are cooled below 220 K, the rigid-lattice lineshapes are obtained. Table III-1 summarizes the proton M_{2D} values determined from the decays generated during the magic echo experiments [32] at temperatures corresponding to the rigid-lattice conditions. Crystalline $TiCuH_{0.94}$ gives the largest M_{2D} even though the other samples contain greater densities of protons per unit volume. This behavior will be related to differences in the distributions of the hydrogen atoms among the available interstitial sites. The $T_{1\rho}$ data are presented in Figure III-3 where the minima indicate the dominance [2,5] of the diffusion contributions. Although the $T_{1\rho}$ recoveries for the $Ti_2CuH_{0.94}$ and a-$TiCuH_{1.4}$ samples were usually exponential within experimental uncertainty, the recoveries for the Ti_2CuH_x samples tended to be nonexponential at most temperatures. Hence, the $T_{1\rho}$ values in Figure III-3 are defined by the time corresponding to the decay to 1/e of the initial amplitude. This procedure permits consistent comparisons among the samples, but it is apparent that the hydrogen diffusion mechanisms are inherently complex in the Ti_2CuH_x samples.

In the rigid-lattice limit it is often possible [2] to determine the hydrogen locations from the proton M_{2D} values providing the structure of the metal atoms is known from x-ray diffraction or another technique. The general formalism for the dipolar contributions to M_{2D} was originally developed by Van Vleck [33]. A generalized version [34] of the Van Vleck formula for a powder sample that takes account of the contributions from inequivalent lattice sites and nonresonant nuclear spins can be written as

$$M_{2D} = C_I \sum_{i,j}^{N} f_i \alpha_{ij} S_{ij} + C_S \sum_{i=1}^{N} f_i S_{ij} \qquad (1)$$

where $C_I = (3/5)(_I\hbar)^2 I(I+1)$ for contributions from other protons with gyromagnetic moment γ_I and spin $I = 1/2$, $\hbar$ is Planck's constant, and $C_S = (4/15)(\gamma_S\hbar)^2 S(S+1)$ for the contributions from unlike nuclei with spin S (here ^{47}Ti, ^{49}Ti, ^{63}Cu, ^{65}Cu) and gyromagnetic moments γ_S. Here, f_i is the fraction of all

TABLE III-1 - EXPERIMENTAL SECOND MOMENTS (M_{2D}) OF THE PROTON LINESHAPES FOR THE TITANIUM-COPPER HYDRIDES.

Sample	Metal Sublattice Structure	T (K)	M_{2D} (G^2)
$TiCuH_{0.94}$	Tetragonal	299	18.5[a]
a-$TiCuH_{1.4}$	Amorphous	80	14.8
$Ti_2CuH_{1.9}$	Orthorhomic(?)	289	13.7
$Ti_2CuH_{2.63}$	Orthorhomic(?)	289	14.3

[a]Experimental error of ± 0.5 G^2 for all samples.

protons located in sites of type i; α_j is the probability of occupation of a j site; and ω_j is the relative number of j sites. Thus, f_i is given by:

$$f_i = \omega_i \alpha_i / \sum_{k=1}^{N} \omega_k \alpha_k \qquad (2)$$

where N is the number of inequivalent proton sites. S_{ij} denotes the lattice sum $\sum_j r_{ij}^{-6}$ where the origin is taken at an i site and the summation extends over all j sites. Similarly, S'_{ij} denotes the sum over metal nuclei with the origin taken at the ith proton site. The theoretical dipolar M_{2D} are calculated for model arrangements of protons within the host metal structure and are compared with the experimental value to determine which model structure gives the best agreement. The proton M_{2D} method for structure determination in a powder is not nearly as powerful as the neutron diffraction techniques, but M_{2D} can be useful in eliminating many trial structures or choosing between alternative models when the neutron diffraction results are incomplete or not available. In practice, the protons should not occupy more than two equivalent sites if unambiguous results are to be obtained from Equation 2.

The structure of crystalline $TiCuD_{0.90}$ has been determined by powder neturon diffraction [22] as shown in Figure III-1. Since the H-atoms only occupy the Ti_4 interstitial sites in the presumably isomorphic TiCuH structure, the M_{2D} expression reduces to a rather simple form, which has been previously evaluated [20] to give a calculated dipolar M_{2D} of 17.8 G^2. The present magic echo experiments on the $TiCuH_{0.94}$ gave $M_{2D} = 18.5 \pm 0.5$ G^2, which is in good agreement with the theoretical value as well as the previous experimental result $M_{2D} = 17.8 \pm 0.8$ G^2 obtained from the lineshape of the proton solid echo [20]. Hence, the TiCuH structure in Figure III-1 seems well established from x-ray and neutron diffraction [6,22], inelastic neutron scattering [7], and the rigid-lattice proton M_{2D} parameters.

Although an orthorhombic structure has been proposed [26] for Ti_2CuH_x, the analyses

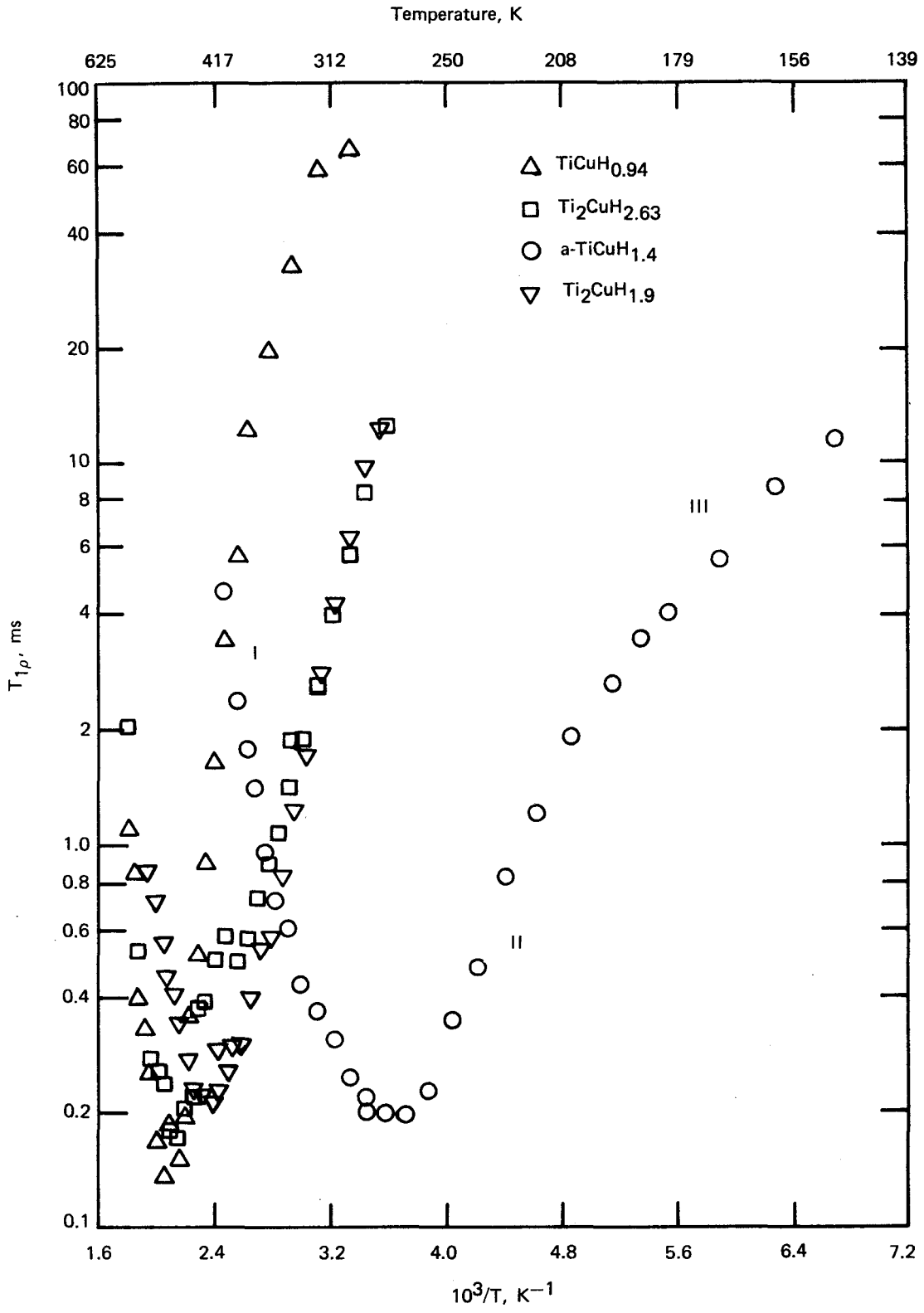

FIGURE III-3 - Proton rotating-frame relatxation times $T_{1\rho}$ at a resonance frequency of 34.5 MHz.

of the x-ray and neutron diffraction patterns have not been completed and the orthorhombic assignment remains tentative. Since interpretations of the diffusion behavior and the electronic properties require at least cursory knowledge of the interstitial sites that are occupied by the H-atoms, a preliminary assessment of the M_{2D} parameters for the Ti_2CuH_x samples has been performed using the data in Table III-1 and some reasonable estimates [26] for the Ti_2CuH_x lattice parameters for the tetragonal and orthorhombic structures. Because of the poor quality of the x-ray diffraction patterns [6,21] for the Ti_2CuH_x samples, the same lattice parameters were used for both $Ti_2CuH_{1.9}$ and $Ti_2CuH_{2.63}$ during the M_{2D} calculations, which reduces the accuracy to some extent and limits quantitive comparisons between the calculated and experimental M_{2D} parameters.

Based upon the Ti_2Cu structure given in Figure III-2 and the inelastic neutron scattering results [27] for $Ti_2CuD_{2.5}$, the three most likely locations for H-atoms are the Ti_4, Ti_4Cu_2, and Ti_2Cu_4 interstitial sites with a preference for the presumably more stable Ti_4 sites. For the tetragonal unit cell of Figure III-2, there are four Ti_4 sites, four Ti_4Cu_2 sites, and two Ti_2Cu_4 sites. The limiting compositions for complete occupancy of the Ti_4 sites and either of the octahedral sites are Ti_2CuH_3 (for Ti_2Cu_4 sites) and Ti_2CuH_4 (for Ti_4Cu_2 sites) if the original tetragonal structure is retained. However, an orthorhombic structure can be generated if H-atoms occupy only half of the Ti_4Cu_2 sites (i.e., those lying along the expanded b-axis) to give the limiting composition Ti_2CuH_3 when the Ti_4 sites are also completely occupied. This particular arrangement of H-atoms of Ti_2CuH_x could provide consistent explanations for the orthorhombic distortion [6,21,35], the presence of vibrational frequencies [27] for hydrogen in both tetrahedral and octahedral sites, and the observed maximum composition $Ti_2CuH_{2.8}$.

The dipolar second moments for $Ti_2CuH_{1.90}$ and $Ti_2CuH_{2.63}$ have been calculated for several distributions of H-atoms in both the tetragonal and orthorhombic structures. Table III-2 summarizes the calculated M_{2D} values where preferential occupancy by the Ti_4 sites has been assumed. During the M_{2D} calculations, the various interstitial sites retain their ideal positions in Figure III-2 (i.e., no further distortions to lower symmetry or puckering of altering hydrogen sites occur) except for the elongation of the b-axis for the orthorhombic structure. Comparisons of the calculated dipolar M_{2D} values with the experimental moments from Table III-1 clearly gives the best agreement for the orthorhombic structure where the Ti_4Cu_2 sites are occupied when $x > 2.0$. Considering the uncertainty in the Ti_2CuH_x lattice parameters, undue emphasis should not be placed upon the comparisons in Table III-2 since other H-atom distributions with lower occupancies of the Ti_4 sites can also give nearly as good agreement in some cases. However, the proton M_{2D} results in Table III-2 are consistent with the orthorhombic structure and the intuitively satisfying preferential filling of the presumably more stable Ti_4 sites. This structure for Ti_2CuH_x provides a reasonable framework for subsequent analysis of the diffusion behavior.

Table III-2 - COMPARISONS OF SOME CALCULATED DIPOLAR SECOND MOMENTS (M_{2D}) FOR THE PROTON LINESHAPES IN $Ti_2CuH_{2.63}$ WHERE THE EXPERIMENTAL VALUES FROM TABLE III-1 WERE OBTAINED WITH MAGIC ECHO SEQUENCE.

Sample	Metal Structure	Occupancy Factors in the Interstitial Sites	Calculated M_{2D} (G^2)	Experimental M_{2D} (G^2)	Deviation Between M_{2D} Values (%)
$Ti_2CuH_{1.9}$	Tetragonal[a]	0.95 Ti_4	16.2	13.7(5)	+18
$Ti_2CuH_{1.9}$	Orthorhombic[b]	0.95 Ti_4	12.7	13.7(5)	-7.3
$Ti_2CuH_{2.63}$	Tetragonal[a]	1.00 Ti_4 & 0.63 Ti_2Cu_4	15.8	14.3(5)	+11
$Ti_2CuH_{2.63}$	Tetragonal[a]	1.00 Ti_4 & 0.315 Ti_4Cu_2	18.5	14.3(5)	+29
$Ti_2CuH_{2.63}$	Orthorhombic[b]	1.00 Ti_4 & 0.63 Ti_4Cu_2*	14.5	14.3(5)	+1.4

[a]Lattice Parameters: a = 0.3064 nm and c = 1.0963 nm

[b]Lattice Parameters: a = 0.306 nm; b = 0.333 nm; c = 1.01 nm

*Only the Ti_4Cu_2 sites along b-axis can be occupied.

Since long-range order is absent in amorphous solids, Equation 1 cannot be directly applied to calculate the dipolar M_{2D} for a-$TiCuH_{1.4}$. Although simulation calculations using Monte Carlo techniques have provided theoretical M_{2D} values in few glassy alloys[36], only qualitative comparison with experiment can be realistically expected. Because local short-range order is present in amorphous $Ti_{1-y}Cu_y$ alloys [28-30], the random packing calculation procedure [36] will be further compromised in these systems. However, the H-atoms predominantly occupy the same sites in the crystalline and amorphous $TiCuH_x$ phases [7]. Table III-1 indicates the experimental M_{2D} for the amorphous a-$TiCuH_{1.4}$ is much closer to the values for the Ti_2CuH_x samples (where Ti_4Cu_2 sites as well as Ti_4 sites are presumably occupied) than for crystalline $TiCuH_{0.94}$. This can be interpreted as suggesting the H-atoms are distributed among similar sites in a-$TiCuH_{1.4}$ and Ti_2CuH_x although greater variation is expected for the amorphous phase. More detailed assessments of the hydrogen distribution in amorphous a-$TiCuH_{1.4}$ are not currently possible.

The NMR techniques have been very successful in evaluating diffusion behavior in many metal-hydrogen systems [2-5]. Since protons are spin 1/2 nuclei without a quadrupole moment to interact with electric field gradients, atomic motion influences proton relaxation only through time dependent modulations of the nuclear dipolar interactions [2]. The diffusion

correlation time τ_c is the parameter that relates nuclear relaxation times to microscopic diffusion processes. The formal connection between the diffusion coefficient D and τ_c is given by:

$$D = K_d \ell^2/\tau_c \quad (3)$$

where K_d is a numerical parameter for symmetry and possible correlation effects, and ℓ is the mean jump distance. Various models have been developed [2] to provide a theoretical framework to τ_c that can reliably describe the diffusion contributions to the nuclear relaxation times. The simple exponential correlation function model of Bloembergen, et al [35], widely called the BPP model, has provided reasonable activation energies (E_a) and relative τ_c values for numerous solids including many metal-hydrogen systems [2,5]. However, the absolute τ_c values from the BPP model may be in error by as much as 50%, and more detailed models have been developed [2]. Unfortunately, these later models are complicated and require explicit computations of lattice summations that are not available [2] except for the simplest cubic lattices. Unless very accurate estimates of D or ℓ are desired, the BPP model is normally adequate to determine the parameters E_a and τ_c with sufficient precision to characterize the major features of diffusion behavior. Since the Ti-Cu hydrides have low symmetry crystal structures and moderately complex diffusion properties [9,20], analyses based solely upon the BPP model have been used to evaluate the diffusion contributions to the proton relaxation time data. This is not a serious limitation since the major intent of these proton NMR measurements has been to understand relative changes in hydrogen diffusion as the crystal structures and interstitial site occupancies are altered. Accurate absolute diffusion rates are not required for these evaluations.

Although most previous determinations of τ_c behavior in metal hydrides have employed [2,5] the diffusion contribution T_{1d} to the proton spin-lattice relaxation times, the low hydrogen mobilities in the Ti-Cu hydrides [9,20] prevented T_1 measurements in the region of the T_1 minima due to the irreversible decompositions of the ternary $TiCuH_x$ and Ti_2CuH_x phases [6,8,9, 20] at much lower temperatures. Without the minimum T_1 values meaningful determination of the τ_c parameters from the T_{1d} data is seriously impaired [2,23]. Consequently, the prior studies [9,20] of diffusion behavior in $TiCuH_{0.94}$ and a-$TiCuH_{1.3}$ had relied upon the proton T_2 and T_{1D} parameters to obtain the E_a values. However, these parameters can only provide order-of-magnitude estimates for τ_c since it is usually difficult to define [2,5] a quantitative correlation between τ_c and the absolute T_2 and T_{1D} values. Furthermore, the T_2 parameters represent atomic mobility at temperatures above the onset of motional narrowing (i.e., $\gamma_I M_{2D}^{1/2} \tau_c \ll 1$) where the weak-collision theory [2,5] of nuclear relaxation is valid. Analysis of the experimental T_{1D} values obtained at temperatures below the motional narrowing region requires the strong collision theory [37] to describe the effects of single atomic jumps on the dipolar order. Thus, comparative analyses of the T_2 and T_{1D} data to deduce the τ_c behavior over the entire temperature ranges were not attempted [9] for the $TiCuH_{0.94}$ and a-$TiCuH_{1.3}$ samples.

The proton $T_{1\rho}$ relaxation times offer several advantages in characterizing diffusion behavior in the $TiCuH_x$ and Ti_2CuH_x samples. First, $T_{1\rho}$ is dominated by the diffusion processes over wide ranges of τ_c to include the slow hopping regime [37] well below motional narrowing (i.e., until τ_c approaches 10^{-3} sec). In the present case the $T_{1\rho}$ data in Figure III-3 represented proton diffusion in the Ti-Cu hydrides as τ_c varied over four orders-of-magnitude from well below motional narrowing (i.e., upper limits of the T_{1D} results) until the decomposition reactions [6,8,9,20] altered the diffusion behavior. The presence of distinct and easily detected minima for the $T_{1\rho}$ data in Figure III-3 allows straightforward identification of unique τ_c values, within the framework of the weak-collision theory [2,31,37], at specific temperatures that are not sensitive to the details of a given model [2] in contract to analyses based upon the T_2 results. The $T_{1\rho}$ data are not particularly sensitive to the various inhomogeneous contributions at zero frequency that can greatly complicate [2,5] the measurement and interpretation of the T_2 parameters. Finally, proton $T_{1\rho}$ data for diffusion in γ-TiH_x are available [31] for direct comparison.

In order to determine the τ_c parameters for the $TiCuH_x$ and Ti_2CuH_x samples, the $T_{1\rho}$ data of Figure III-3 were first corrected for small conduction electron contributions (primarily, at the lowest temperatures) with the relation $T_{1\rho}{}^{-1} = (T_{1\rho})_d{}^{-1} + (T_{1e})^{-1}$ where the same hyperfine interaction constants are assumed [38] to the proton T_1 and $T_{1\rho}$ relaxation processes. The average $(T_{1e}T)^{-1/2}$ values from Figure III-4 were used to estimate the T_{1e} contributions at each temperature. Since the spin-locking fields H_1 for the $T_{1\rho}$ data in Figure III-4 obey $H_1{}^2 >> M_{2D}/3$, the weak collision theory [2,37] remains applicable even at the temperatures below motional narrowing. Using the BPP model for the dipolar correlation function, $\tau_c{}^{-1}$ is obtained from the formula given by Korn and Goren [31]

$$(T_{1\rho})_d{}^{-1} = 4/3(T_{1\rho})_{d,min}^{-1} \left[\frac{3y}{y^2+4} + \frac{5y}{y^2+a^2} + \frac{2y}{y^2+4a^2}\right] \quad (8)$$

where $(T_{1\rho})_{d,min}$ is the minimum value of $(T_{1\rho})_d$, $y = (\omega_1\tau_c)^{-1}$, $\omega_1 = \gamma_H H_1$, a ω_o/ω_1, and ω_o is the proton resonance frequency in radians/sec. The temperature dependences of the $\tau_c{}^{-1}$ values, which are proportional to D through Equation 7, for the $TiCuH_x$ and Ti_2CuH_x samples are plotted in Figures III-5 and III-6. The E_a values and preexponential factors A, where $\tau_c{}^{-1}(T) = A \exp(-E_a/k_B T)$, are summarized in Table III-3 along with the temperature for $(T_1\rho)_{d,min}$, the $\tau_c{}^{-1}$ value at 300 K, and the limits for Arrhenius behavior of τ_c values.

When the $\tau_c{}^{-1}$ values for crystalline $TiCuH_{0.94}$ and amorphous a-$TiCuH_{1.4}$ are compared with $\tau_c{}^{-1}$ results of Korn and Goren [31] for γ-$TiH_{1.90}$, all of the major observations from the earlier studies involving the T_2 and T_{1D} measurements [9,20] are completely confirmed. First, a much slower hydrogen diffusion rate below 550 K and a larger E_a value are obtained for $TiCuH_{0.94}$ compared to the results for TiH_x as is clearly evident from Figure III-5 and Table III-3. The greatly enhanced diffusion rate in amorphous

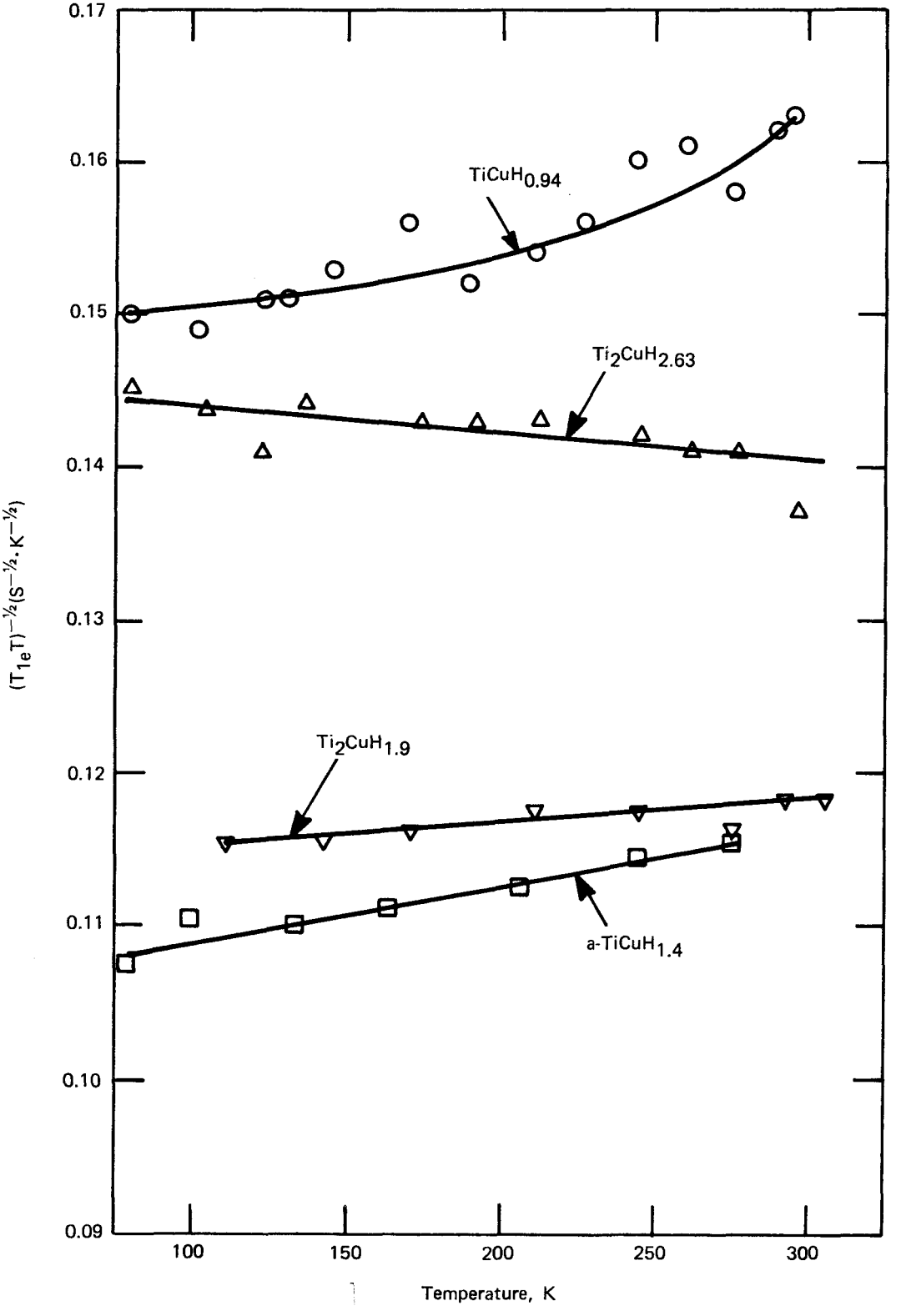

FIGURE III-4 - Temperature dependent behavior of $(T_{1e}T)^{-1/2}$ parameters.

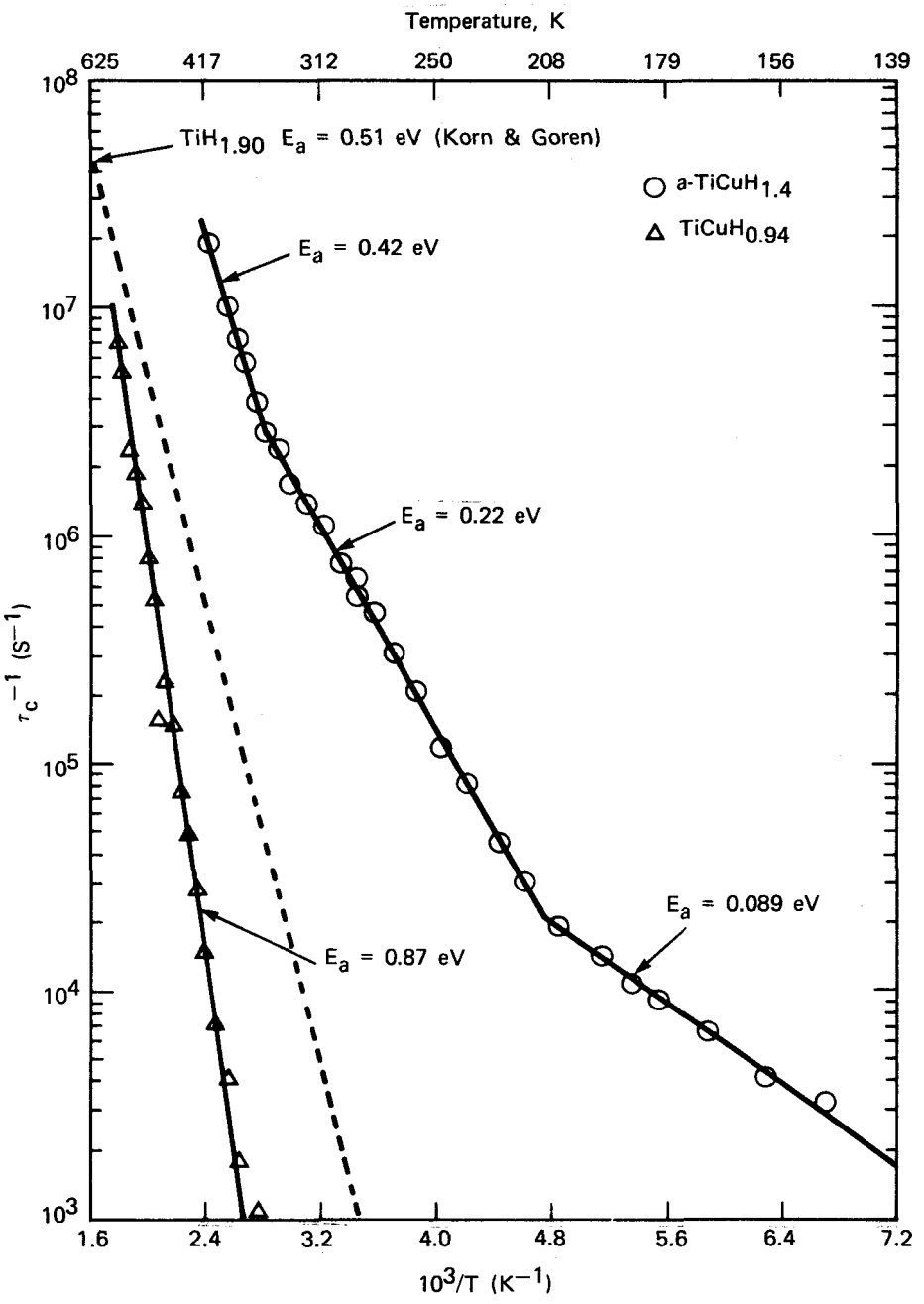

FIGURE III-5 - Temperature dependences of diffusion jump rates τ_c^{-1} for crystalline and amorphous $TiCuH_x$ that were obtained from $T_{1\rho}$ data. Also shown are the results from $T_{1\rho}$ measurements for $TiH_{1.90}$ by Korn and Goren [30].

Table III-3 - SUMMARY OF HYDROGEN DIFFUSION PARAMETERS FOR Ti_yCuH_x AND TiH_x THAT HAVE BEEN DERIVED FROM PROTON $T_{1\rho}$ RELAXATION TIMES WITH THE EXPONENTIAL CORRELATION TIME MODEL WHERE $\tau_c^{-1}(T) = A \exp(-E_a/k_BT)$.

Hydride	Structure	Temperature for $T_{1\rho}$ Minimum	τ_c^{-1}(300 K) (s^{-1})	A (s^{-1})	E_a (eV)	Temperature Range	Reference
$TiCuH_{0.94}$	Tetragonal	483 K	1.1	4.4×10^{14}	0.87 ± 0.03	360 - 560 K	Present work
a-$TiCuH_{1.4}$	Amorphous	275 K	-	2.8×10^{12}	0.42 ± 0.03	355 - 415 K	Present work
			8.0×10^{5}	-	0.22 ± 0.02	210 - 355 K	
			-	-	0.089 ± 0.01	150 - 210 K	
$Ti_2CuH_{1.9}$	Orthorhombic	424 K	5.5×10^{3}	2.5×10^{10}	0.40 ± 0.03	280 - 520 K	Present work
$Ti_2CuH_{2.63}$	Orthorhombic	470 K	-	2.7×10^{12}	0.64 ± 0.04	425 - 540 K	Present work
			5.2×10^{3}	-	0.29 x 0.02	280 - 405 K	
$TiH_{1.81}$	fcc	∿410 K	3.9×10^{3}	1.29×10^{12}	0.51 ± 0.01	270 - 660 K	Korn & Goren
$TiH_{1.90}$	fcc	∿430 K	2.4×10^{3}	0.793×10^{12}	0.51 ± 0.01	270 - 660 K	Korn & Goren

a-$TiCuH_{1.4}$ is also unmistakable where its τ_c^{-1} (300 K) is 8×10^5 larger than the corresponding value for $TiCuH_{0.94}$ and more than 200 times larger than τ_c^{-1} (300 K) for $TiH_{1.81}$. The E_a values for a-$TiCuH_{1.4}$ are smaller than the diffusion activation energies for TiH_x and crystalline $TiCuH_{0.94}$. While τ_c^{-1} for crystalline $TiCuH_{0.94}$ and γ-TiH_x follow Arrhenius behavior over the entire measured temperature ranges, distinct non-Arrhenius temperature dependence is observed for a-$TiCuH_{1.4}$ with three E_a values representing the τ_c^{-1} results between 150 K and 415 K.

The hydrogen diffusion behavior for the crystalline Ti_2CuH_x samples are compared to $TiCuH_{0.94}$ and γ-$TiH_{1.90}$ in Figure III-6. The proton mobilities for the Ti_2CuH_x samples are somewhat greater than observed in $TiCuH_{0.94}$ but not quite as rapid as in γ-$TiH_{1.50}$ when the temperature exceeds about 350 K. However, the smaller E_a values for the Ti_2CuH_x samples produce slightly faster mobilities (i.e., larger τ_c^{-1} values) at temperatures below 350 K. Whereas the τ_c^{-1} values for $Ti_2CuH_{1.9}$ follow Arrhenius behavior over the entire range of the T_1 measurements, two E_a values are required for the $Ti_2CuH_{2.63}$ sample.

The differences in hydrogen diffusion properties in the $Ti_{1-y}Cu_yH_x$ system are believed to illustrate the importance of metal atom structure and hydrogen site occupancy on the microscopic jump processes.

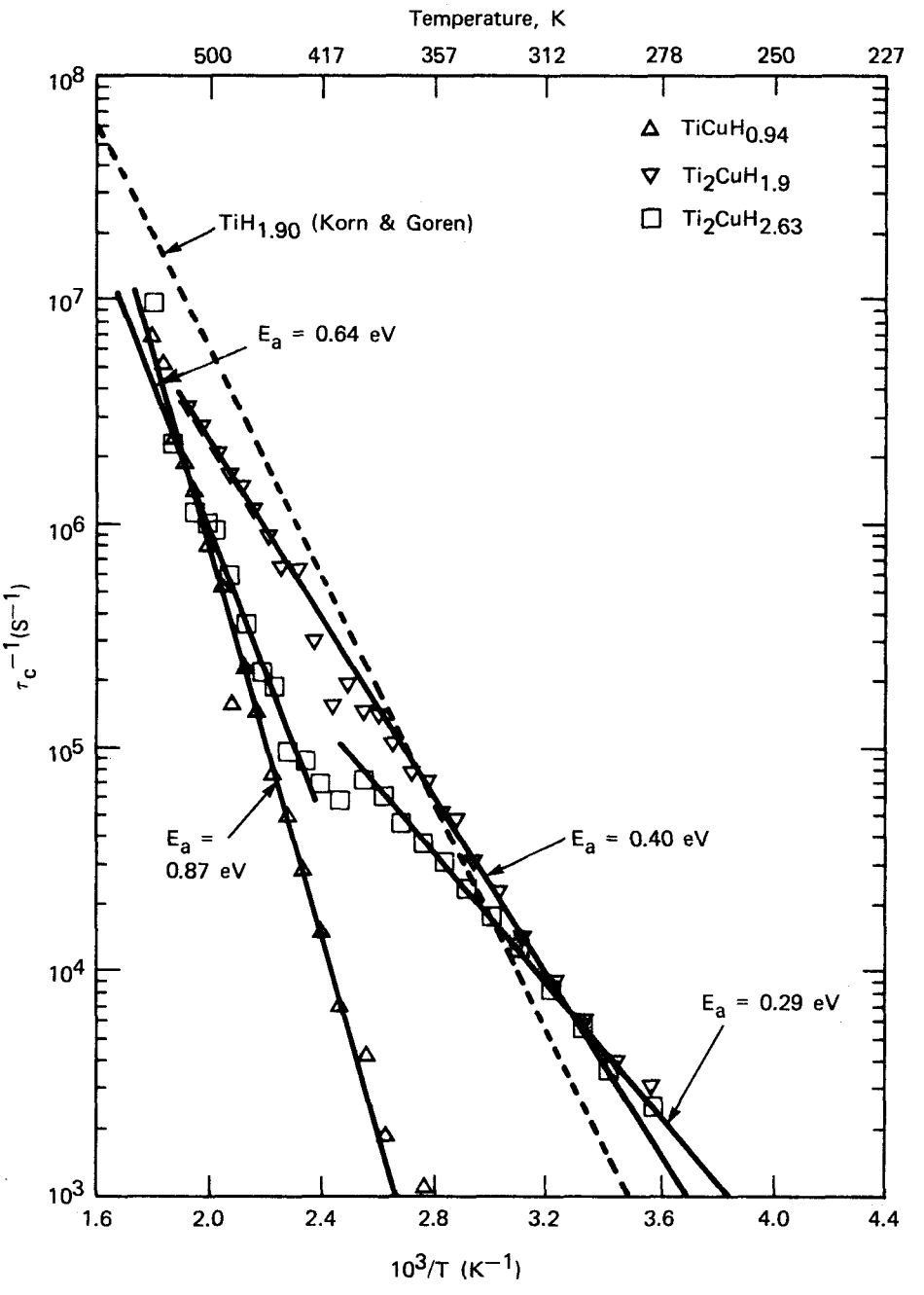

FIGURE III-6 - Temperature dependences of diffusion jump rates τ_c^{-1} for crystalline $TiCuH_{0.94}$, $Ti_2CuH_{1.9}$, and $Ti_2CuH_{2.63}$ that were obtained from $T_{1\rho}$ data. Also shown are the results from $T_{1\rho}$ measurements for $TiH_{1.90}$ by Korn and Goren [30].

The slowest diffusion rate and largest E_a values occur for $TiCuH_{0.94}$ where the crystal structure (see Figure III-1) presumably requires [5,20] the H-atoms to jump the high barriers [39] between the nearest neighbor tetrahedral sites within the plane of the double Ti-atom layer. The lower E_a values for γ-TiH_x and $Ti_2CuH_{1.9}$ reflect smaller barriers [39] for jump paths through octahedral interstitial sites. It is interesting to note that in the hydrides where H-atoms occupy one type of site (i.e., the Ti_4 sites in γ-TiH_x, $TiCuH_{0.94}$, and $Ti_2CuH_{1.9}$) the Arrhenius relation is obeyed throughout the range of the $T_{1\rho}$ measurements. However, the τ_c^{-1} results for $Ti_2CuH_{2.63}$, where the protons occupy both Ti_4 and Ti_4Cu_2 sites according to the previous M_{2D} analysis, show distinct non-Arrhenius behavior where two E_a values are obtained. It is speculated that the smaller value (i.e., E_a = 0.29 eV) may correspond to jumps among the octahedral sites while the larger E_a is a composite energy [9,40] which represents complex jump paths that involve both the octahedral intermediate sites as well as direct tetrahedral-tetrahedral jumps. In $Ti_2CuH_{1.9}$, the Ti_4Cu_2 sites are presumably vacant and H-atoms in the Ti_4 sites can diffuse without interference by jumping through the normally empty Ti_4Cu_2 sites to give a tendency towards a channel pathway along the c-axis. However, the occupancy of most Ti_4Cu_2 sites in $Ti_2CuH_{2.63}$ would tend to block this channel and the H-atom would often be required to perform direct tetrahedral-tetrahedral jumps before finding a vacant Ti_4CuH_2 site. Of course, assuming H-atoms in the Ti_4Cu_2 sites are more mobile gives an increased probability that a vacant octahedral site becomes available for occupancy by a H-atom from a neighboring Ti_4 site. Consequently, this rather complex diffusion process should yield an intermediate E_a to the activation energies for $TiCuH_{0.94}$ and $Ti_2CuH_{1.9}$. Figure III-6 shows that this appears to be the situation above 400 K where the absolute τ_c^{-1} parameters for $Ti_2CuH_{2.63}$ are only slightly larger than than values in $TiCuH_{0.94}$, which is qualitatively consistent with impedance of the more direct jump paths proposed for $Ti_2CuH_{1.9}$. Unfortunately, more complete information on the relative interstitial site occupancies as well as independent estimates of activation energies for the several elementary jump barriers are required before a detailed analysis can be presented. There are simply too many unspecified parameters to give anything other than the present very qualitative description. However, the experimental results in Figure III-6 and Table III-3 are at least consistent with this tentative explanation.

The three E_a values for a-$TiCuH_{1.4}$ from the proton $T_{1\rho}$ measurements are in good agreement with earlier values [9] from the T_2 and T_{1D} data for the a-$TiCuH_{1.3}$ samples at corresponding temperatures. The $T_{1\rho}$ experiments are not sufficiently sensitive to the very slow diffusion contributions to determine whether a smaller E_a exists below 150 K as was suggested by the T_{1D} experiments. If the arguments of the preceding paragraph are extended to a-$TiCuH_x$, three (or four) types of interstitial sites are being occupied by protons in the amorphous phase. The low E_a values imply that direct tetrahedral to tetrahedral jumps are not important hydrogen diffusion pathways in the amorphous phase. Alternative diffusion pathways are permitted in the disordered structure and are probably responsible

for the greatly enhanced diffusion in a-$TiCuH_x$ relative to crystalline $TiCuH_{0.94}$. However, the amorphous phase irreversibly decomposes [6,8,9] at such a low temperature (i.e., about 425 K during the NMR experiments) that the possible contributions of tetrahedral to tetrahedral jumps to the overall hydrogen diffusion process are never observed. If amorphous a-$TiCuH_x$ has retained much of the short range order, which has been indicated in the a-$Ti_{1-y}Cu_y$ alloys [28-30], some neighboring Ti_4 sites should exist in a-$TiCuH_x$ and be occupied by H-atoms. However, the microscopic diffusion processes are probably even more complicated than the proposed mechanism for crystalline $Ti_2CuH_{2.63}$. Nevertheless, the sharp breaks in the temperature dependence of τ_c^{-1} for a-$TiCuH_{1.4}$ in Figure III-5 as well as in the previous T_2 and T_{1D} data [9] suggest that only a relative few distinct changes in the diffusion process occur rather than a gradual variation from a quasi-continuous distribution of processes with slightly different activation energies. The latter situation would be expected for a completely random arrangement of proton environments in the amorphous hydride. Since only relatively few processes apparently determine the proton diffusion behavior in a-$TiCuH_x$, the retention of short range order in the amorphous hydride may have limited the number of allowed H-atom jump pathways. A brief, qualitative description of the diffusion processes that is similar to the mechanism proposed above for $Ti_2CuH_{2.63}$ has been given [9]. Unfortunately, additional knowledge of the types and distributions of occupied H-sites as well as E_a values are again required before a detailed interpretation of hydrogen diffusion behavior in a-$TiCuH_x$ is attempted.

Although the proton NMR experiments have provided unequivocal evidence for orders-of-magnitude enhancement of the hydrogen diffusion (with accompanying E_a decreases) in amorphous a-$TiCuH_{1.3\pm0.1}$ relative to crystalline $TiCuH_{0.94}$, recent studies of amorphous alloys with low-hydrogen concentrations [13,16-18] indicated that hydrogen mobilities are comparable or even slower (i.e., with larger E_a values) than obtained in essentially identical crystalline alloys. These apparent discrepancies can be reconciled if some reasonable conditions are imposed. First, it is probably safe to assume that at low concentrations most H-atoms in an amorphous alloy are trapped either at defect sites or small voids although this does not appear to have been experimentally demonstrated. A hydrogen in such a trap is more tightly bound than an H-atom in the normal interstitial site and should also have a higher activation barrier [3,4] for any subsequent diffusive jump. However, at large hydrogen concentrations (i.e., in a-$TiCuH_{1.3\pm0.1}$) most H-atoms will occupy a much wider distribution of interstitial sites which may include many sites where the diffusion E_a values are much smaller than the jump paths allowed for sites occupied in the corresponding crystalline structure. Consequently, an enhanced hydrogen diffusion rate with smaller E_a values than are observed in the crystalline phase becomes possible. This is assumed to be the situation for a-$TiCuH_{1.3\pm0.1}$. However, the constraints that are imposed on hydrogen diffusion by the $TiCuH_{1.0}$ crystal structure, whose τ_c^{-1} (300 K) in Table III-3 is more than three orders-of-magnitude smaller than the corresponding values for γ-TiH_x and Ti_2CuH_x, probably produce an exceptionally

large differtial between amorphous and crystalline structures. In very recent studies of internal friction in hydrogen doped amorphous a-$Zr_{0.76}Ni_{0.24}$, Agyeman, et al [19] found the relaxation times, which is inversely proportional to D, to decrease and the activation energies to decrease with the addition of more hydrogen. Hence, their results are in complete accord with the present description. Proton lineshape measurements [15] in crystalline and amorhpous $ZrPdH_x$ with $x \geq 1.9$ have also indicated greater hydrogen mobility in the amorphous hydride phases. However, extensive and systematic studies of hydrogen diffusion behavior in several amorphous and corresponding crystalline hydrides are needed to establish the specific contributions of short range order and interstitial site occupancies on the basic diffusion mechanisms.

References

I. Low temperature research

1. J. W. Pyper, E. M. Kelly, J. G. Magistad, R. T. Tsugawa, P. E. Roberts, P. C. Souers, UCRL52391, Lawrence Livermore National Laboratory, (1978).

2. L. M. Dorfman and H. C. Mattraw, J. Phys. Chem., 57, 723 (1953).

3. H. C. Mattraw, C. F. Pachucki, L. M. Dorfman, J. Chem. Phys., 20, 926 (1952).

4. L. M. Dorfman and F. J. Shipko, J. Phys. Chem., 59, 1110 (1955).

5. S. O. Thompson and O. A. Schaeffer, J. Phys. Chem., 80, 553 (1958).

6. O. A. Schaeffer and S. O. Thompson, Rad. Res., 10, 671 (1959).

7. Quantum Mechanics, Inc., P. O. Box 1211, Tracy, CA, 95376.

8. Private communication (Ed Walter, Quantum Mechanics, Inc., 1981).

9. S. C. Lind, Radiation Chemistry of Gases, (Reinhold, New York, 1961), p. 88.

10. S. C. Lind, Ibid., p. 6

11. P. C. Souers, E. M. Fearon, R. T. Tsugawa, Cryogenics, 21, 667 (1981).

12. G. T. McConville (to be published).

13. M. Allen and S. F. Wong, Phys. Rev. Letters, 41, 1791 (1978).

14. Rates are product of velocities determined from energy in eV assigned times the reaction cross section found in C. F. Barnett et al, ORNL-5206 and ORNL-5207, Oak Ridge National Laboratory, (1977).

15. J. R. Hiskes et al. (to be published).

16. Mound Facility Activities in Chemical and Physical Research: January-June 1981, MLM-2884 (December 15, 1981), pp. 12-15.

17. R. E. Ellefson, R. W. Baker, and J. T. Gill, "Gaseous Mixtures of Hydrogen, Deuterium, and Helium-3 Produced by a Partial-Pressure Mixing System," MLM-2574 (November 14, 1978).

18. T. L. Ibbs and K. E. Grew, Proc. Phys. Soc. London, 43, 142 (1931).

19. A de Troyer, A. van Itterbeck, and G. J. van den Berg, Physica (Utrecht), 16, 669 (1950).

20. K. E. Grew, Proc. R. Soc. London, Ser. A 189, 402 (1947).

21. A. van Itterbeck and A. de Troyer, Physica (Utrecht), 16, 329 (1950).

22. A. van Itterbeck, O. van Paemel, and J. van Lierde, Physica (Utrecht), 13, 231 (1947).

23. J. H. Dymond and B. J. Alder, J. Chem. Phys. 51, 309 (1969).

24. H. M. Lin and R. L. Robinson, Jr., J. Chem. Phys. 54, 52 (1971).

25. R. Ahlrichs, R. Penco, and G. Scoles, Chem. Phys. 19, 119 (1977).

26. C. H. Chen, P. E. Siska, and Y. T. Lee, J. Chem. Phys. 59, 601 (1973).

27. E. A. Mason, J. Chem. Phys. 23, 49 (1955).

II. Separation research

1. Mound Facility Activities in Chemical and Physical Research: July-December 1981, MLM-2892 (May 3, 1982), p. 14.

2. G. P. Flynn, R. V. Hanks, N. A. Lemaire, and J. Ross, J. Chem. Phys., 30, 154 (1963).

3. J. T. K. Kao, W. Ruska, and R. Kobayashi, Rev. Sci. Instru., 39, 824 (1968).

4. S. B. K. Sun and T. S. Storvick, J. Chem. Eng. Data, 24, 88 (1979).

5. M. de Haas, Comm. Leiden No. 12, (1894).

6. H. Stakelbeck, Z. Ges. Kalte - Ind., 40, 33 (1933).

7. A. F. Benning and W. H. Markwood, Jr., Refrig. Eng., 37, 243 (1939).

8. J. H. Awbery and E. Griffiths, Proc. Phys. Soc., London, 48, 372 (1936).

9. Mound Facility Activities in Chemical and Physical Research: January-June 1981, MLM-2884 (December 15, 1981), p. 19.

10. W. M. Rutherford and K. W. Laughlin, Science, 211, 1054 (1981).

11. Mound Facility Activities in Chemical and Physical Research: July-December 1981, MLM-2892 (May 3, 1982), p. 18

12. Mound Facility Activities in Chemical and Physical Research: January-June 1981, MLM-2884 (December 15, 1981), p. 21.

13. T. Marrero and E. Mason, J. Phys. Chem. Ref. Data, 1, 3 (1972); T. R. Marrero and E. A. Mason, Advances in Atomic and Molecular Physics, Vol. 6, (Academic Press, New York, NY, 1970), Chapter 4, p. 156.

14. A. E. Loiko, B. A. Ivakin and P. E. Seutin, Sov. Phys.- Tech Phys., 19, 434 (1974).

15. B. A. Kalinen and P. E. Suetin, Heat Transfer - Sov. Res., 7, 146 (1975).

16. P. S. Arora, H. L. Robjohns and P. J. Dunlop, Physica, 95A, 561 (1979).

17. W. Hogervorst, Physica, 51, 59 (1971).

18. C. J. Zwakhals and K. W. Reus, Physica, 1006, 231 (1980).

19. Mound Facility Activities in Chemical and Physical Research: January-June 1978, MLM-2555 (September 18, 1978), p. 36.

20. S. Weissman, Proc. of the 4th Symp. on Thermophysical Properties, ASME, New York, 1966, pp. 360-65.

21. a) J. Kestin, St. Ro, and W. Wakeham, Physica, (Utrecht), 58, 165 (1972). b) J. Kestin and E. A. Mason, AIP Conf. Proc. 11, 137 (1973).

22. R. Ahlrichs, R. Penco, and G. Scoles, Chem. Phys., 19, 119 (1977).

23. K. M. Smith, A. M. Rulis, G. Scoles, R. A. Aziz, and V. Nain, J. Chem. Phys., 67, 152 (1977).

24. Mound Facility Activities in Chemical and Physical Research: July-December 1981, MLM-2892 (May 3, 1982), P. 23.

25. Mound Facility Activities in Chemical and Physical Research: January-June 1981, MLM-2884 (December 15, 1981), p. 25.

26. P. E. Suetin, B. A. Kalinen and A. E. Loiko, Sov. Phys.-Techn. Phys., 15, 1349 (1971).

27. J. C. Liner and S. Weissman, J. Chem. Phys., 56, 2288 (1972).

28. V. P. S. Nain and S. C. Saxena, Appl. Sci. Res., 23, 121 (1970).

29. a) A. S. Kalelkar and J. Kestin, J. Chem. Phys., 52, 4248 (1970); b) G. C. Maitland and E. B. Smith, J. Chem. Soc., Faraday Trans. I, 70, 1191 (1974); c) D. W. Gough, G. P. Matthews and E. B. Smith, J. Chem. Soc., Faraday Trans. I, 72, 645 (1976).

30. J. Kestin, S. T. Ro and W. Wakeham, Physica (Utrecht), 58, 165 (1972).

31. J. Kestin and E. A. Mason, AIP Conf. Proc. 11, 137 (1973).

32. W. L. Taylor, J. Chem. Phys., 64, 3344 (1976).

33. W. L. Taylor, J. Chem. Phys., 72, 4973 (1980).

34. J. Kestin, W. Wakeham and K. Watanabe, J. Chem. Phys., 53, 3773 (1970).

35. J. Kestin, H. E. Khalifa and W. A. Wakeham, Physica, 90A, 215 (1978).

36. Mound Facility Activities in Chemical and Physical Research: January-June 1979, MLM-2654 (October 29, 1979).

37. Mound Facility Activities in Chemical and Physical Research: July-December 1981, MLM-2892 (May 3, 1982), p. 29.

38. Mound Facility Activities in Chemical and Physical Research: July-December 1981, MLM-2892 (May 3, 1982), p. 31.

39. Mound Facility Activities in Chemical and Physical Research: July-December 1980, MLM-2809 (April 10, 1981), p. 35.

40. R. Helbing, W. Gaide and H. Pauly, Zeit. f. Physik, 208, 215 (1968).

41. W. R. Eckelt, B. Schimpke and K. Schügerl, Zeit. f. Physikal. Chem. Neue Folge, 68, 266 (1969).

42. H. J. Beier, Zeit. f. Physik., 196, 185 (1966).

43. F. Pirani and F. Vecchiocattivi, J. Chem. Phys., 66, 372 (1977).

44. R. S. Grace, W. M. Pope, D. L. Johnson, and J. G. Skofronick, Proc. Int. Conf. on Physics of Electronic and Atomic Collisions, Washington Univ. Press, 1975, p. 1019.

45. J. H. Dymond and B. J. Alder, J. Chem. Phys., 54, 52 (1971).

46. H. M. Lin and R. L. Robinson, Jr., J. Chem. Phys., 54, 52 (1971).

47. E. A. Mason and W. E. Rice, J. Chem. Phys., 59, 601 (1973).

48. C. H. Chen, P. E. Siska, and Y. T. Lee, J. Chem. Phys., 59, 601 (1973).

49. R. A. Aziz, P. W. Riley, U. Buck, G. Maneke, J. Schleusener, G. Scoles, and U. Valbusa, J. Chem. Phys., 71, 2637 (1979).

50. P. S. Arora, H. L. Robjohns, and P. J. Dunlop, Physica, 95A, 561 (1969).

51. G. C. Maitland and W. A. Wakeham, Mol. Phys., 70, 482 (1979).

52. M. Keil, J. T. Slankas, and A. Kuppermann, J. Chem. Phys., 70, 482 (1979).

53. E. Glueckauf, "Isotope Separation by Chromatographic Methods," H. London (ed.), Separation of Isotopes, William Clowes and Sons Limited, 1961, p. 232.

III. Metal hydride studies

1. G. L. Silver in The Rare Earths in Modern Science and Technology, Vol. 2, G. B. McCarthy, J. J. Rhyne, and H. B. Silber (eds.), Plenum, New York, 1980, p. 605.

2. R. M. Cotts, in Hydrogen in Metals I, G. Alefeld and J. Volkl (eds.), Springer-Verlag, Berlin, 1978, p. 227.

3. J. Volkl and G. Alefeld, in Diffusion in Solids, Recent Developments, A. S. Nowick and J. J. Burton (eds.), Academic Press, New York, 1975, p. 231.

4. J. Volkl and G. Alefeld, in Hydrogen in Metals I, Galefeld and J. Volkl (eds.), Springer-Verlag, Berlin, 1978, p. 321.

5. R. C. Bowman, Jr., in Metal Hydrides, G. Bambakidis (ed.), Plenum, New York, 1981, p. 109.

6. A. J. Maeland, in Hydrides for Energy Storage, A. F. Andressen and A. J. Maeland (eds.), Pergamon, Oxford, 1978, p. 447

7. J. J. Rush, J. M. Rowe, and A. J. Maeland, J. Phys. F: Metal Phys., 10, L283 (1980).

8. A. J. Maeland, L. E. Tanner, and G. G. Libowitz, J. Less-Common Met., 74, 279 (1980).

9. R. C. Bowman, Jr. and A. J. Maeland, Phys. Rev. B, 24, 2328 (1981).

10. F. H. M. Spit, J. W. Drijver, and S. Radelaar, Zeit. Physk. Chem. N.F., 116, 225 (1979).

11. F. H. M. Spit, J. W. Drijver, W. C. Turkenburg, and S. Radelaar, J. de Physique Colloque C8, 41, C8-890 (1980).

12. F. H. M. Spit, J. W. Drijver, W. C. Turkenburg, and S. Radelaar, in Metal Hydrides, G. Bambakidis (ed.), Plenum, New York, 1981, p. 345.

13. Y. Takagi and K. Kawamura, Trans. Japan Inst. Metals, 22, 677 (1981).

14. T. Kajitani, H. Kaneko, and M. Kirabayashi, Sci. Rep. RITU, 29A, 210 (1981).

15. R. C. Bowman, Jr., M. J. Rosker, and W. L. Johnson, to be published.

16. B. S. Berry and W. C. Pritchet, J. Appl. Phys., 52, 1865 (1981).

17. B. S. Berry and W. C. Pritchet, Phys. Rev. B., 24, 2299 (1981).

18. B. S. Berry and W. C. Pritchet, Scripta Met., 15, 637 (1981).

19. K. Agyeman et al., J. de Physique Colloque C5, 42, C5-535 (1981).

20. R. C. Bowman, Jr., A. Attalla, and A. J. Maeland, Solid State Commun., 27, 501 (1978).

21. A. J. Maeland and G. G. Libowitz, J. Less-Common Met., 74, 295 (1980).

22. A. Santoro, A. Maeland, and J. J. Rush, Acta Cryst. B, 34, 3059 (1978).

23. C. Korn and D. Zamir, J. Phys. Chem. Solids, 31, 489 (1969); 34, 725 (1973).

24. L. D. Bustard, R. M. Cotts, and E. F. Seymour, Phys. Rev. B., 22, 15 (1980).

25. R. Kadel and A. Weiss, Ber. Bunsenges. Phys. Chem., 82, 1290 (1978).

26. A. Santoro, A. J. Maeland, and J. J. Rush, unpublished results.

27. J. J. Rush and A. J. Maeland, unpublished results.

28. M. Sakata, N. Cowlam, and H. A. Davies, J. Phys. F: Metal Phys., 9, L235 (1979).

29. M. Sakata, N. Cowlam, and H. A. Davies, J. de Phys. Colloque C8, 41, C8-190 (1980).

30. D. Raoux, J. F. Sadoc, P. Lagarde, A. Sadoc, and A. Fontaine, J. de Physique Colloque C8, 41, C8-207 (1980).

31. C. Korn and S. D. Goren, Phys. Rev. B, 22, 2727 (1980).

32. R. C. Bowman, Jr. and W. K. Rhim, J. Magn. Res. 49, 93 (1982)

33. J. H. Van Vleck, Phys. Rev., 74, 1168 (1948).

34. R. G. Barnes, W. C. Harper, S. O. Nelson, D. K. Thome, and D. R. Torgeson, J. Less-Common Met., 49, 483 (1976).

35. N. Bloembergen, E. M. Purcell, and R. V. Pound, Phys. Rev., 73, 679 (1948).

36. I. Bakonyi, L. Takacs, and K. Tompa, Phys. Stat. Sol. (b), 103, 489 (1981).

37. D. C. Ailon in Advances in Magnetic Resonance, Vol. 5, J. S. Waugh (ed.), Academic, New York, 1971, p. 177.

38. M. Goldman, Spin Temperature and Nuclear Magnetic Resonance in Solids Clarendon, Oxford, 1970.

39. C. L. Bisson and W. D. Wilson, in Proc. Int. Conf. Effects of Hydrogen Behavior in Materials, A. W. Thompson (ed.), Petroleum Engineers, New York, 1976, p. 416; C. F. Melius and T. H. Upton, Bull. Am. Phys. Soc., 23, 234 (1978).

40. P. A. Fedders, Phys. Rev., B, 18, 1055 (1978).

DO NOT MICROFILM

Distribution

EXTERNAL

TIC-4500, UC-4 and UC-22 (194)
J. R. Blair, DOE/Office of Health and Environmental Re
J. Burnett, DOE/Office of Basic Energy Sciences
R. K. Flitcraft, Monsanto Research Corporation
K. Gschneidner, Iowa University, Ames, Iowa
N. Haberman, DOE/Division of Nuclear Energy
H. N Hill, DOE/Dayton Area Office
J. N. Maddox, DOE/Office of Health and Environmental Research
L. R. Morss, Argonne National Laboratory
C. W. Roos, Monsanto, St. Louis
H. A. Schneiderman, Monsanto, St. Louis
F. D. Stevenson, DOE/Office of Basic Energy Sciences
L. Thompson, University of Minnesota
E. L. Venturini, Sandia National Laboratories, Albuquerque
D. White, University of Pennsylvania
Monsanto Reports Library, R2C, St. Louis

INTERNAL

G. C. Abell
W. R. Amos
L. R. Baird
R. C. Bowman
D. Cain
R. E. Ellefson
C. W. Huntington
B. E. Jepson
B. R. Kokenge
G. T. McConville
D. A. Menke
E. D. Michaels
W. M. Rutherford
G. C. Shockey
G. L. Silver
W. L. Taylor
R. E. Vallee
W. R. Wilkes
L. J. Wittenberg
R. W. York
Document Control
Library (15)
Publications

Published by Information Services
Stephen L. Nowka, Editor